# Supporting Information

## Inducing Antiferromagnetism in a Vinylene-linked 2D Covalent Organic Framework via Metal Complex Anchoring

Satyapriya Nath,[ab] Stefan Trenker,[cd] Jeebanjyoti Mohapatra,[ab] Valentin Zimmermann,[c] Loknath Patro,[ab] Isha,[e] Suresh Bommakanti,[*a] B. L. Bhargava,[ab] Arvind K. Yogi[*e] and Bishnu P. Biswal[*abf]

[a]School of Chemical Sciences
National Institute of Science Education and Research (NISER) Bhubaneswar
Jatni, Khurda, Odisha, 752050, India

[b]Homi Bhabha National Institute (HBNI)
Training School Complex, Anushakti Nagar, Mumbai, 400094, India

[c]Max Planck Institute for Solid State Research
Heisenbergstraße 1, 70569 Stuttgart, Germany

[d]Department of Chemistry
University of Munich (LMU)
Butenandtstraße 5-13, 81377 München, Germany

[e]UGC-DAE Consortium for Scientific Research
University Campus, Khandwa Road, Indore (M.P.) 452001, India

[f]Center for Interdisciplinary Sciences
National Institute of Science Education and Research (NISER) Bhubaneswar
Jatni, Khurda, Odisha, 752050, India

E-mail: bp.biswal@niser.ac.in , akyogi@csr.res.in , sureshpgcb@gmail.com

**Table of Contents**

## Section S-1: Experimental and Synthetic Procedures

**Materials:**

All the chemicals and solvents were received as reagent grade and used without further purification. The starting materials were commercially available and purchased from ABCR Chemicals, Germany.

**General instrumentation and methods:**

**Powder X-ray diffraction (PXRD)** patterns were collected at room temperature on a Stoe Stadi P diffractometer [Cu-$K_{\alpha 1}$, Ge (111)] in Debye-Scherrer geometry. The samples were measured inside a sealed glass capillary (1.0 mm) with spinning for improved particle statistics. Molecular modelling of the **TMT-PPy** COF was carried out using the BIOVIA Materials Studio suite, and the structure and unit cell parameters were relaxed using force fields (Forcite, universal force fields with Ewald electrostatic and van der Waals summations method). The unit cell of the experimentally obtained PXRD pattern of **TMT-PPy** COF was then refined in the $2\theta$ range 2-40° in the Reflex module of the BIOVIA Materials Studio, with fixed atom coordinates. The obtained structural models were checked for bond length and bond angle consistency in the structure.

**Fourier transform infrared (FT-IR)** spectra were recorded in attenuated total reflection (ATR) geometry on a PerkinElmer UATR equipped with a diamond crystal. The spectra were background corrected. Finally, the FT-IR data were reported with a wave number ($cm^{-1}$) scale.

**Thermogravimetric analyses (TGA)** were carried out on a TG50 analyzer (Mettler-Toledo) and an SDT Q600 TG-DTA analyzer in the air at a heating rate of 5 ºC $min^{-1}$ in the temperature range of 25-800 ºC.

**UV-visible diffuse reflectance (UV-DRS) absorption spectra** were collected on a Cary 5000 spectrometer (referenced to barium sulfate). Absorption spectra were calculated from the reflectance data using the Kubelka-Munk function.

**Elemental analysis (EA)** was carried out with an Elementar Vario EL (Elementar Analysensysteme, Hanau, Germany).

**Inductively coupled plasma atomic emission spectroscopy (ICP-OES)** was done on a VARIAN VISTA RL simultaneous spectrometer (Agilent Technologies, Santa Clara, California, USA) with a CCD-detector.

**Scanning electron microscopy (SEM)** measurements were executed with a Merlin Compact field effect SEM (FESEM) with a GEMINI-I electron column, Zeiss Pvt. Ltd., Germany.

**Transmission electron microscopy (TEM)** images and EDS spectra was acquired with a Philips CM30 ST, and JEOL 2100F HRTEM. The samples were prepared dry onto a copper lacey carbon grid (Plano).

**Nitrogen ($N_2$) adsorption analyses** were performed at 77 K on a Quantachrome Instruments Autosorb iQ MP automatic volumetric instrument. The COF samples were outgassed for 12 h at 120 °C under the vacuum before the gas adsorption studies. The surface areas were evaluated using the Brunauer-Emmett-Teller (BET) model applied between $P/P_0$ values of 0.05 and 0.2 for mesoporous COFs. The pore size distributions were calculated using the Quenched Solid-State Density Functional Theory (QSDFT) cylindrical-slit adsorption kernel for carbon implemented in the ASiQwin software v 3.01.

**Solution NMR** measurements were performed on a JEOL ECZ 400S 400 MHz spectrometer and Bruker advance III 400 MHz Spectrometer. ($^1$H measurements were performed in 5 mm NMR tubes using a deuterium field lock. An appropriate number of accumulations have been made to achieve a sufficient signal-to-noise ratio. Chemical shifts ($\delta$) are given in parts per million (ppm) relative to tetramethylsilane (TMS); coupling constant J is given in Hertz (Hz). $(CD_3)_2SO$ [$\delta$ ($^1$H) = 2.50 ppm] and $CDCl_3$ [$\delta$ ($^1$H) = 7.26 ppm] were used as solvents lock and internal standards.

**Solid-state NMR spectra** was recorded on a Bruker Advance III 400 MHz spectrometer (magnetic field 9.4 T). For ss-NMR spectroscopy, the samples were packed in 4 mm $ZrO_2$ rotors spun in a Bruker WVT BL4 double resonance MAS probe. The chemical shift was referenced relative to TMS ($^{13}$C) and $CH_3NO_2$ ($^{15}$N) as an external standard. The spinning rate was 12-14 kHz for $^{13}$C NMR and 8 kHz for $^{15}$N measurements. A standard cross-polarization sequence with a 2 ms ramped contact pulse was used for $^{13}$C, and a total of 4096-8192 scans were routinely accumulated. $^{15}$N solid-state NMR spectra were obtained with ramped cross-polarization and contact pulses of 3-8 ms optimized for the best signal. Both $^{13}$C and $^{15}$N measurements were performed at conditions of high-power broadband proton decoupling (SPINAL 64), with the spectral conditions being optimized for the shortest relaxation delay by measuring the $^1$H T1 relaxation time.

**Electron paramagnetic resonance (EPR) spectra** were recorded on Bruker Biospin AG spectrometer using X-band frequency region on powder samples at room temperature.

**Synthetic Procedures:**

**Synthesis of IrCp*Cl(2-phenylpyridine):**

Following a literature procedure,[1] pentamethylcyclopentadienyl iridium dichloride $[IrCp^*Cl_2]_2$ (60.0 mg, 0.075 mmol, 1.0 eq.) and NaOAc (24.7 mg, 0.301 mmol, 4.0 eq.) were dissolved in dichloromethane (12 mL). 2-phenyl pyridine (26.2 mg, 0.166 mmol, 2.2 eq.) was added, and the reaction mixture was stirred at room temperature overnight. The solvent was removed under reduced pressure, and the residue was washed with n-hexane (4 x 3 mL) and dried in a vacuum. IrCp*Cl@PPy was obtained as a bright orange crystalline powder (59.1 mg, 0.151 mmol, 76%).

**Synthesis of TMT-PPy COF:**

A Schlenk tube was charged with 2,4,6-trimethyl-1,3,5-triazine (TMT, 6.35 mg, 0.05 mmol), 6-(4-formyl phenyl)pyridine-3-carbaldehyde (PPy, 15.8 mg, 0.075 mmol), 0.3 mL mesitylene, 0.6 mL 1,4-dioxane, 0.20 mL trifluoroacetic acid, and 0.025 mL acetonitrile. The tube was flash-frozen at 77 K in a liquid $N_2$ bath, evacuated, and sealed. The reaction mixture was sonicated for 10 min and then heated to 150 °C for 72 h. The solid was collected, washed with acetone and methanol, neutralized by 0.1 M $NH_4OH$ solution in aqueous methanol (50 wt%), and then washed with methanol in a Soxhlet extractor for 12 h. Finally, the material was subjected to supercritical $CO_2$ drying and degassing under a dynamic vacuum to yield **TMT-PPy** COF.

**Synthesis of IrCp*Cl@TMT-PPy COF:**

To a suspension of **TMT-PPy** (24 mg, 0.012 mmol) in methanol (3 mL), pentamethylcyclopentadienyl iridium dichloride $[IrCpCl_2]_2$ (24 mg, 0.03 mmol) and sodium acetate (6 mg, 0.073 mmol) was added, and the resulting suspension was stirred at room temperature for 6 h. After the reaction time had elapsed, the solid was collected by filtration and washed with methanol. Finally, the material in wet condition was subjected to supercritical $CO_2$ drying to yield **IrCp*Cl@TMT-PPy** COF.

**Synthesis of TMT-PP COF:**

The TMT-PP COF was prepared by following the literature procedure.[2] In a typical procedure, a Schlenk tube was charged with 2,4,6-trimethyl-1,3,5-triazine (TMT, 6.0 mg, 0.049 mmol), 4,4'-biphenyldicarbaldehyde (PP, 15.36 mg, 0.075 mmol), and 0.45 mL mesitylene, 0.45 mL 1,4-dioxane, 0.025 mL acetonitrile, and 0.20 mL trifluoroacetic acid. The tube was flash-frozen at 77 K (liquid $N_2$ bath), evacuated, and sealed. The reaction mixture was sonicated and heated at 150 °C for 72 h to give the **TMT-PP** COF. The solid was collected, washed with acetone and methanol, neutralized by 0.1M $NH_4OH$ solution in aqueous methanol (50 wt%), and then washed with methanol in a Soxhlet extractor

for 12 h. Finally, the material was subjected to supercritical $CO_2$ drying and degassing at 120 °C under a dynamic vacuum.

**Synthesis of TTA-PPy COF:**

A Pyrex tube was charged with 2,4,6-tris(4-aminophenyl)-1,3,5-triazine (TTA, 15 mg, 0.042 mmol), 6-(4-formyl phenyl)pyridine-3-carbaldehyde (PPy, 13.4 mg, 0.063 mmol), and 1.33 mL mesitylene, and 0.66 mL 1,4-dioxane. The reaction mixture was sonicated for 5 minutes and degassed, and 0.10 mL acetic acid (6 M) was added. The tube was sealed under inert gas and heated at 130 °C for 90 h. The solid was collected, washed with DMF, THF, acetone, and methanol, and then washed with methanol in a Soxhlet extractor for 12 h. Finally, the material was subjected to supercritical $CO_2$ drying to yield **TTA-PPy** COF.

**Synthesis of IrCp*Cl@TTA-PPy COF:**

To a suspension of TTA-PPy COF (50 mg, 0.12 mmol) in DMF (8 mL) was added pentamethylcyclopentadienyl iridium dichloride $[IrCpCl_2]_2$ (25 mg, 0.03 mmol) and sodium acetate (10 mg, 0.12 mmol). The resulting suspension was stirred at room temperature at 150 rpm for 22 h. The solid was collected by filtration and washed with acetone, ethanol, water, and methanol. Finally, the material in wet condition was subjected to supercritical $CO_2$ drying to yield **IrCp*Cl@TTA-PPy** COF.

## Section S-2: Powder X-ray diffraction and structural analysis

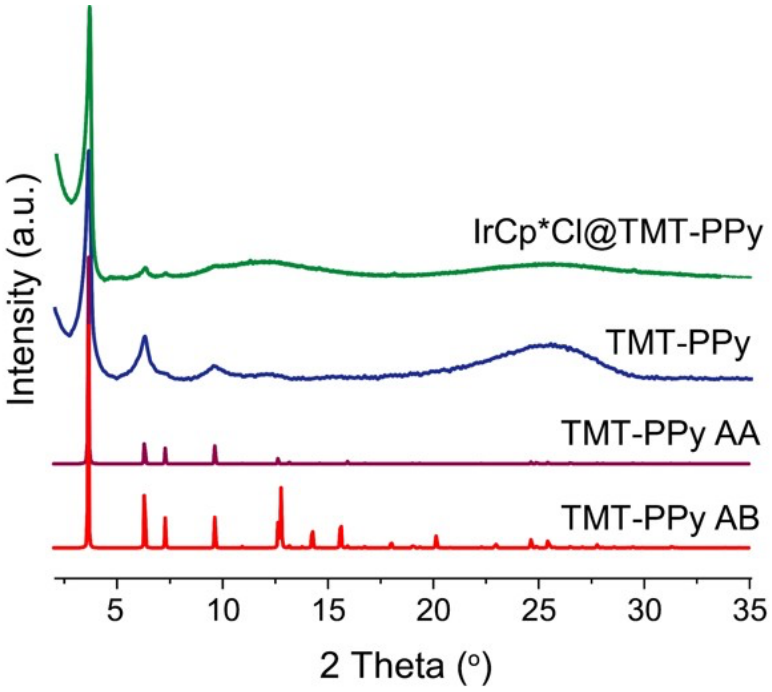


**Figure S1.** Experimental PXRD patterns (CuK$_\alpha$-1.54 Å) of **TMT-PPy** and **IrCp*Cl@TMT-PPy** COFs, compared with simulated patterns of AA and AB stacking models of TMT-PPy COF.

PXRD patterns of **TMT-PPy** COF revealed a crystalline nature with the first intense peak at $2\theta = 3.6°$, corresponding to the 100 plane. The broad peak in the range of $2\theta = 24 - 27°$, corresponding to the 001 plane, signified π-π stacking between the vertically stacked layers. The structure was modelled in 2D eclipsed mode. The simulated PXRD pattern of a fully eclipsed AA structure matched well with the experimentally obtained PXRD pattern. Further, the lattice parameters of **TMT-PPy** COF were extracted by Pawley refinement in the hexagonal space group *P*3, with the lattice parameters $a = b = 27.97$ Å, $c = 3.61$ Å, $\alpha = \beta = 90°$ and $\gamma = 120°$.

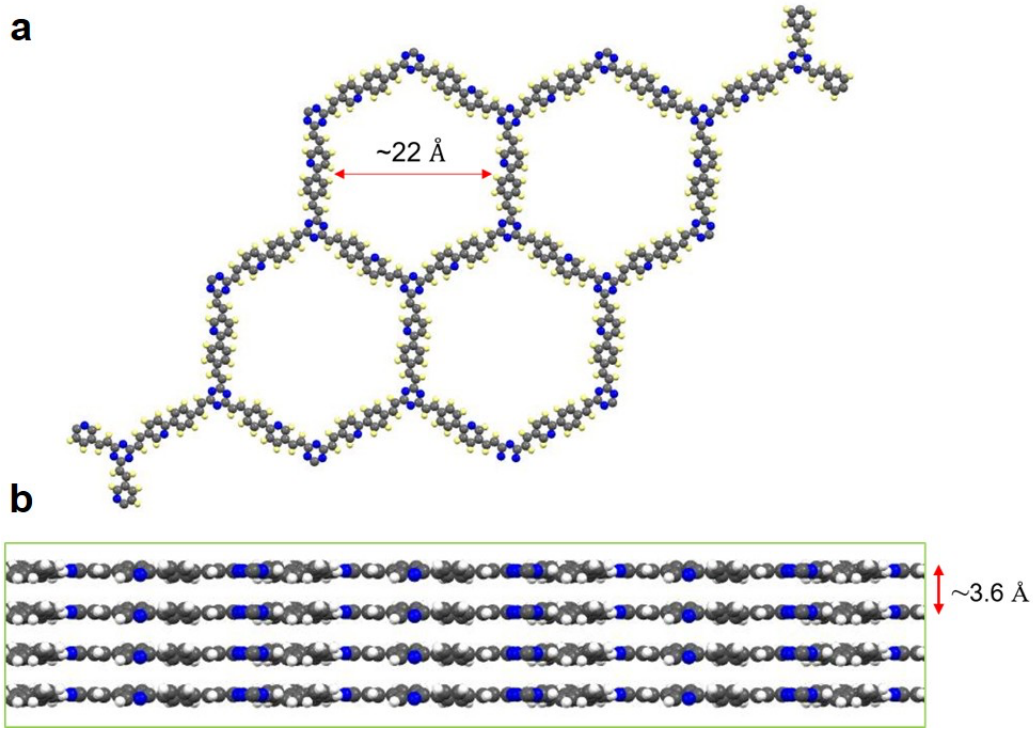


**Figure S2.** a) Representation of AA-stacking model showing pore aperture of ca. ~22 Å and b) corresponding side view of the **TMT-PPy** COF exhibiting the π-π stacking distance of 3.6 Å.

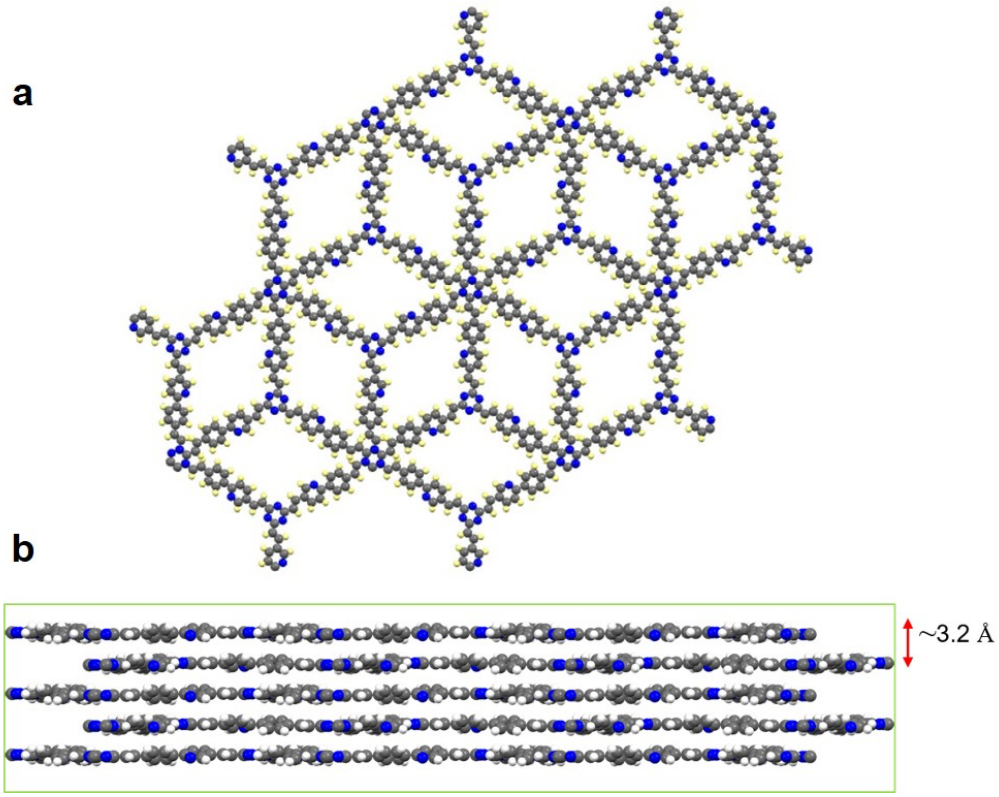


**Figure S3.** a) Representation of AB-stacking model and b) corresponding side view of the **TMT-PPy** COF exhibiting the π-π stacking distance of 3.2 Å.

## Section S-3: FT- IR and NMR spectra

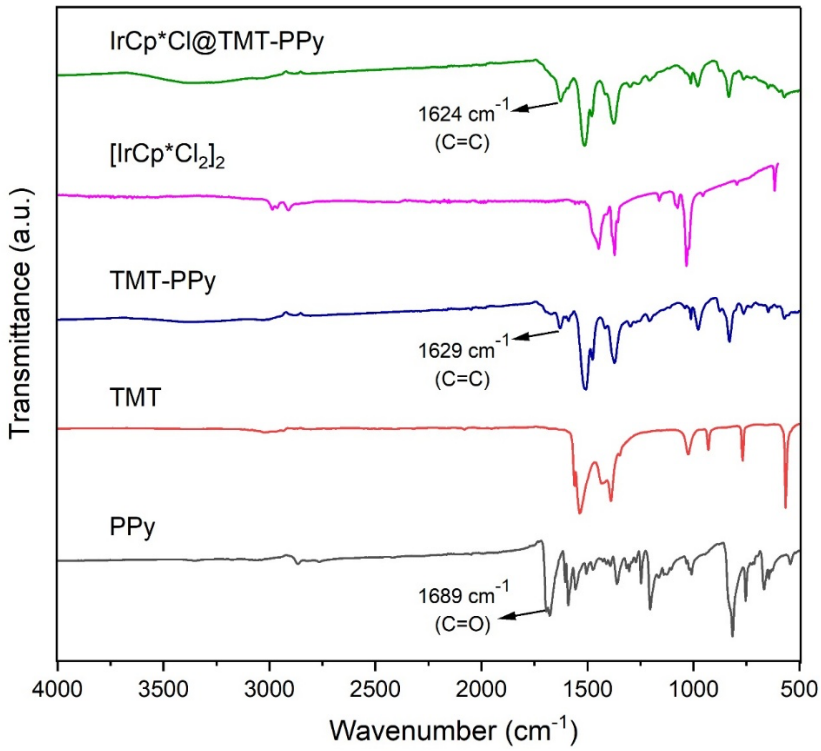


**Figure S4**. Fourier transform infrared (FT-IR) spectroscopy of PPy, TMT monomers, and $[IrCp^*Cl_2]_2$ complex compared to **TMT-PPy** and **IrCp*Cl@TMT-PPy** COFs.

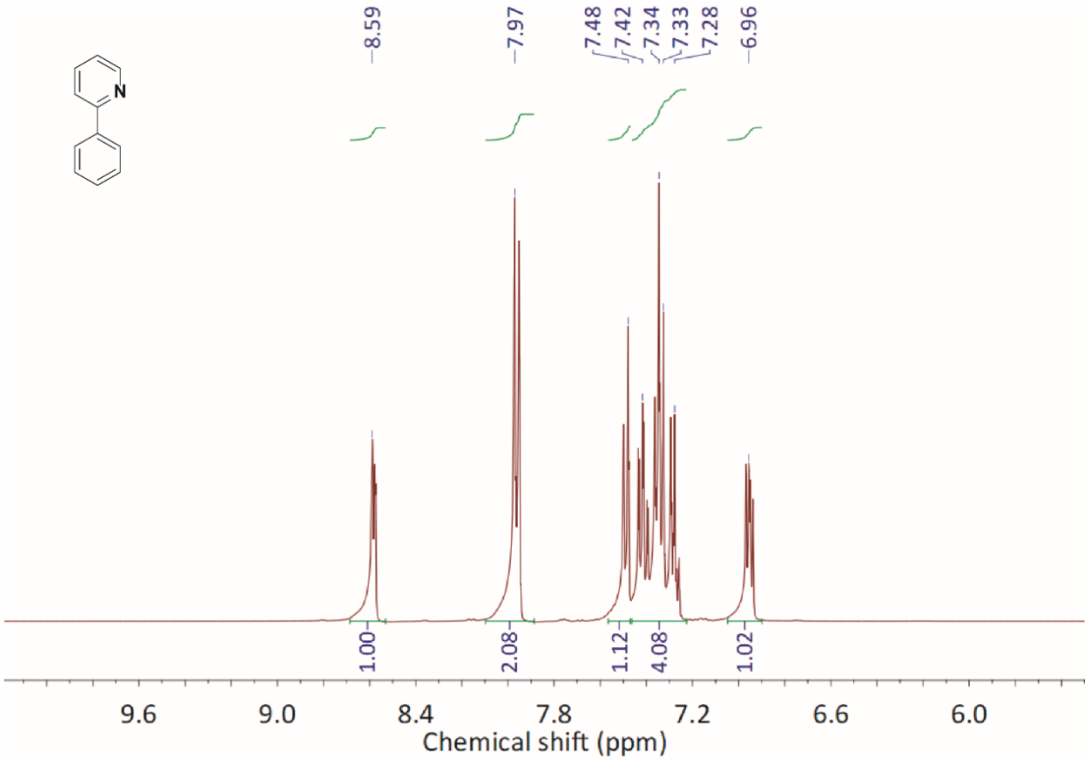


**Figure S5.** $^1$H NMR spectrum of 2-phenylpyridine ligand (400 MHz).

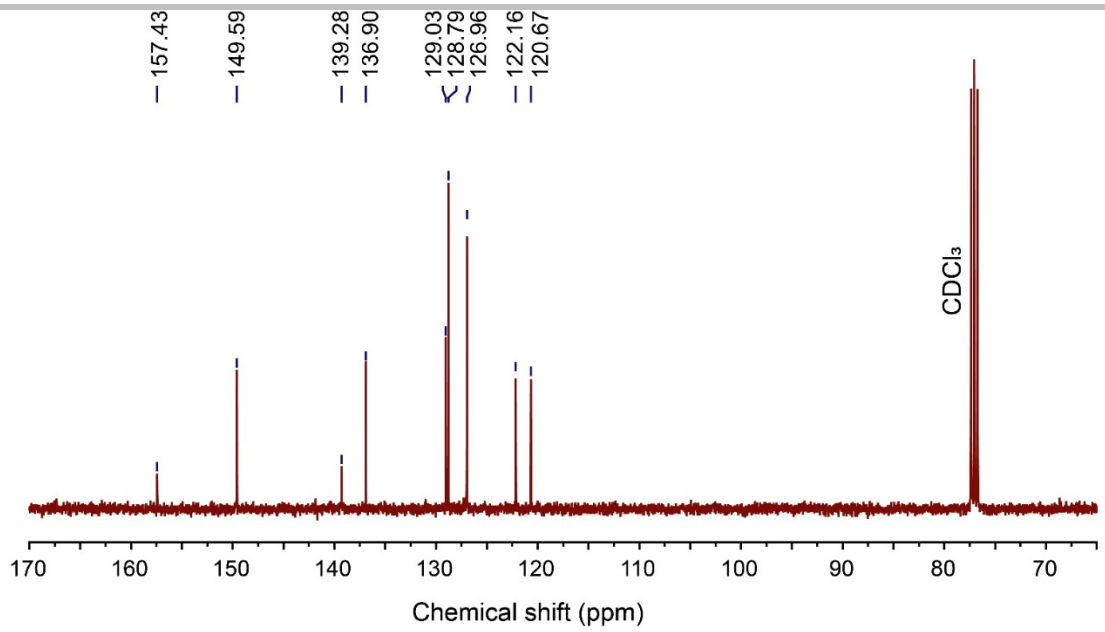


**Figure S6.** $^{13}C$ NMR spectrum of 2-phenylpyridine ligand (400 MHz).

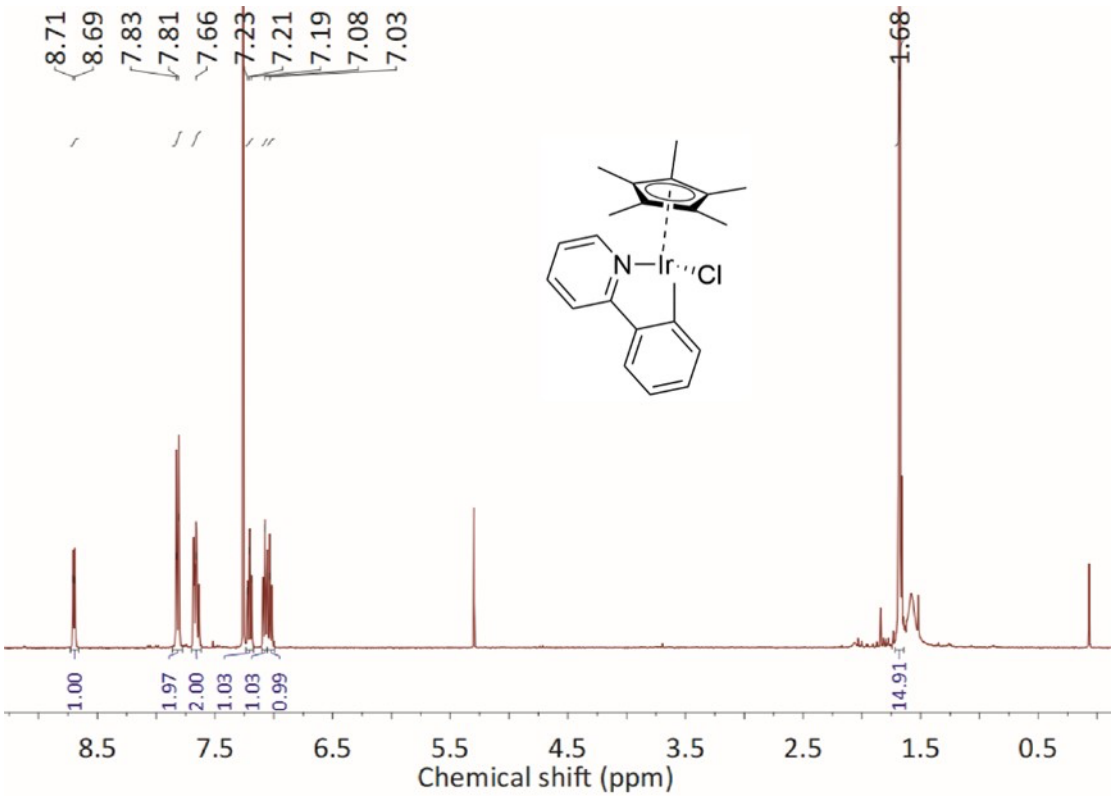


**Figure S7.** $^{1}H$ NMR spectrum of IrCp*Cl(2-phenylpyridine) (*model compound for metallated COF*) in $CDCl_3$ (400 MHz).

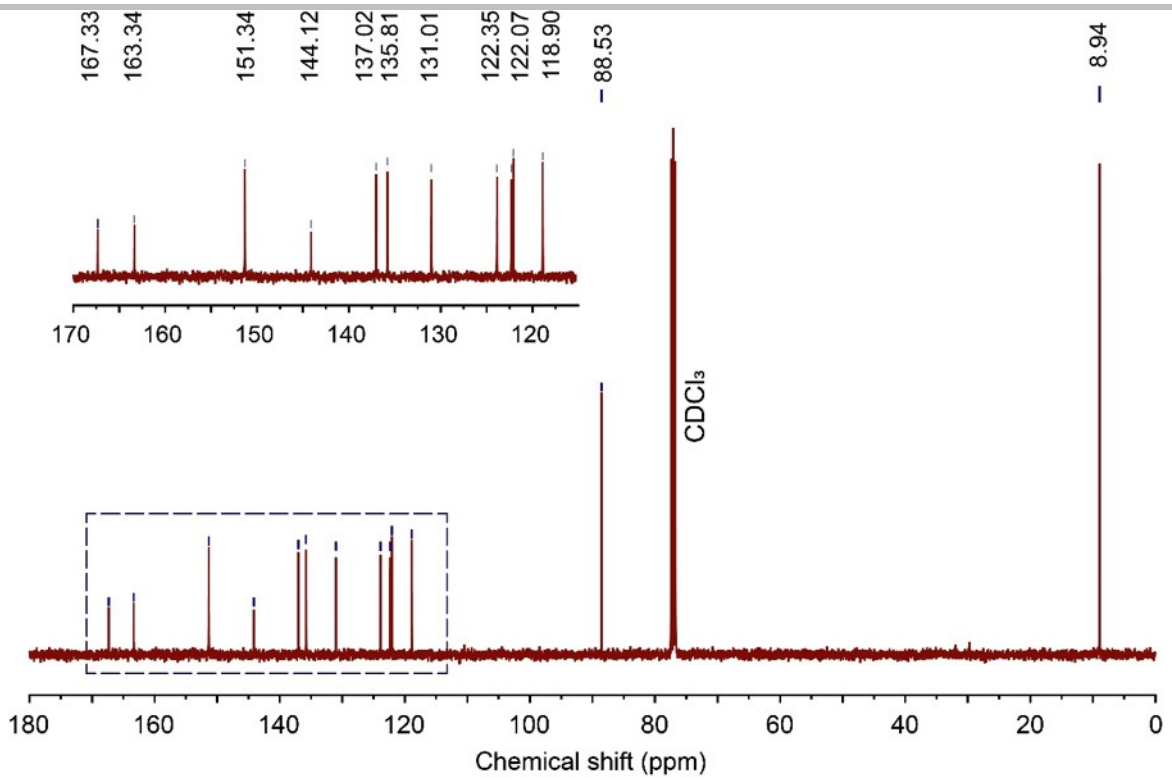


**Figure S8.** $^{13}C$ NMR spectrum of IrCp*Cl(2-phenylpyridine) (400 MHz) in $CDCl_3$.

**Table S1:** ICP-OES analysis for the metallated COF:

| S.No. | Method | Elements determined | Result (wt%) |
|---|---|---|---|
| **1** | ICP-OES | Ir | 22.49 |

## 2D NMR spectra

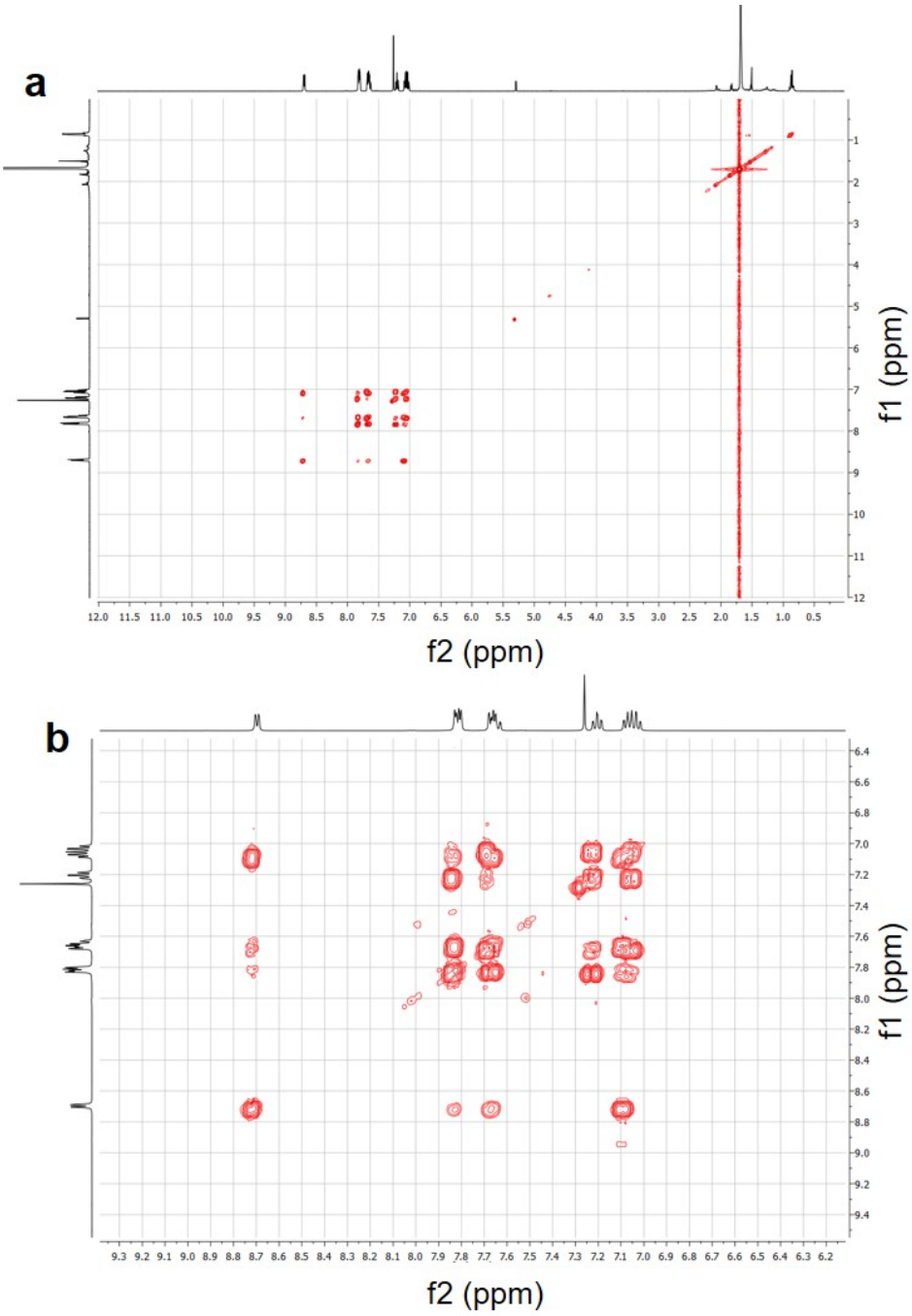


**Figure S9.** $^{1}$H-COSY spectrum of IrCp*Cl(2-phenylpyridine) in $CDCl_3$. The lower image shows an enlargement of the aromatic region.

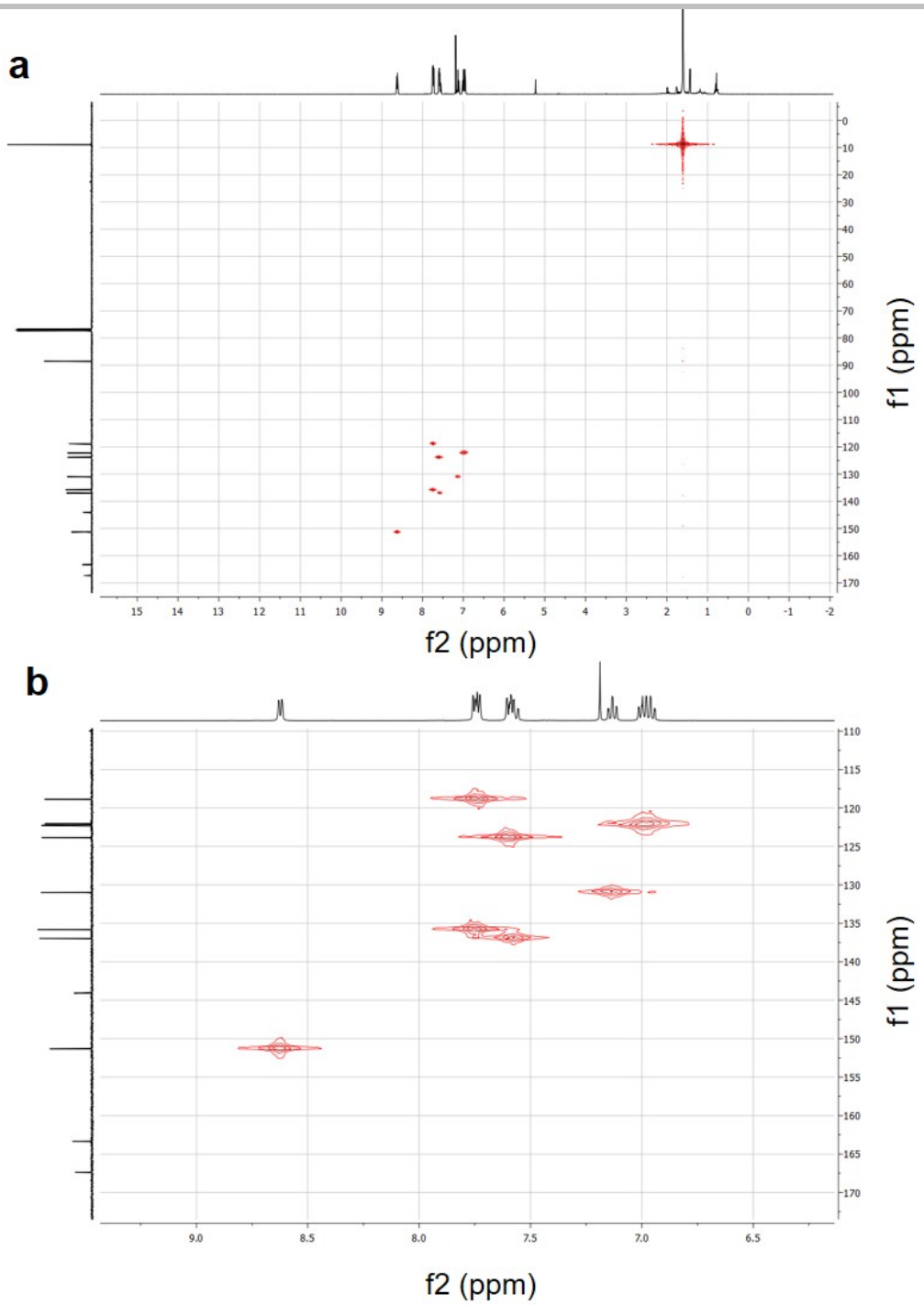


**Figure S10.** HSQC spectrum of IrCp*Cl(2-phenyl pyridine) in $CDCl_3$. The lower image shows an enlargement of the aromatic region.

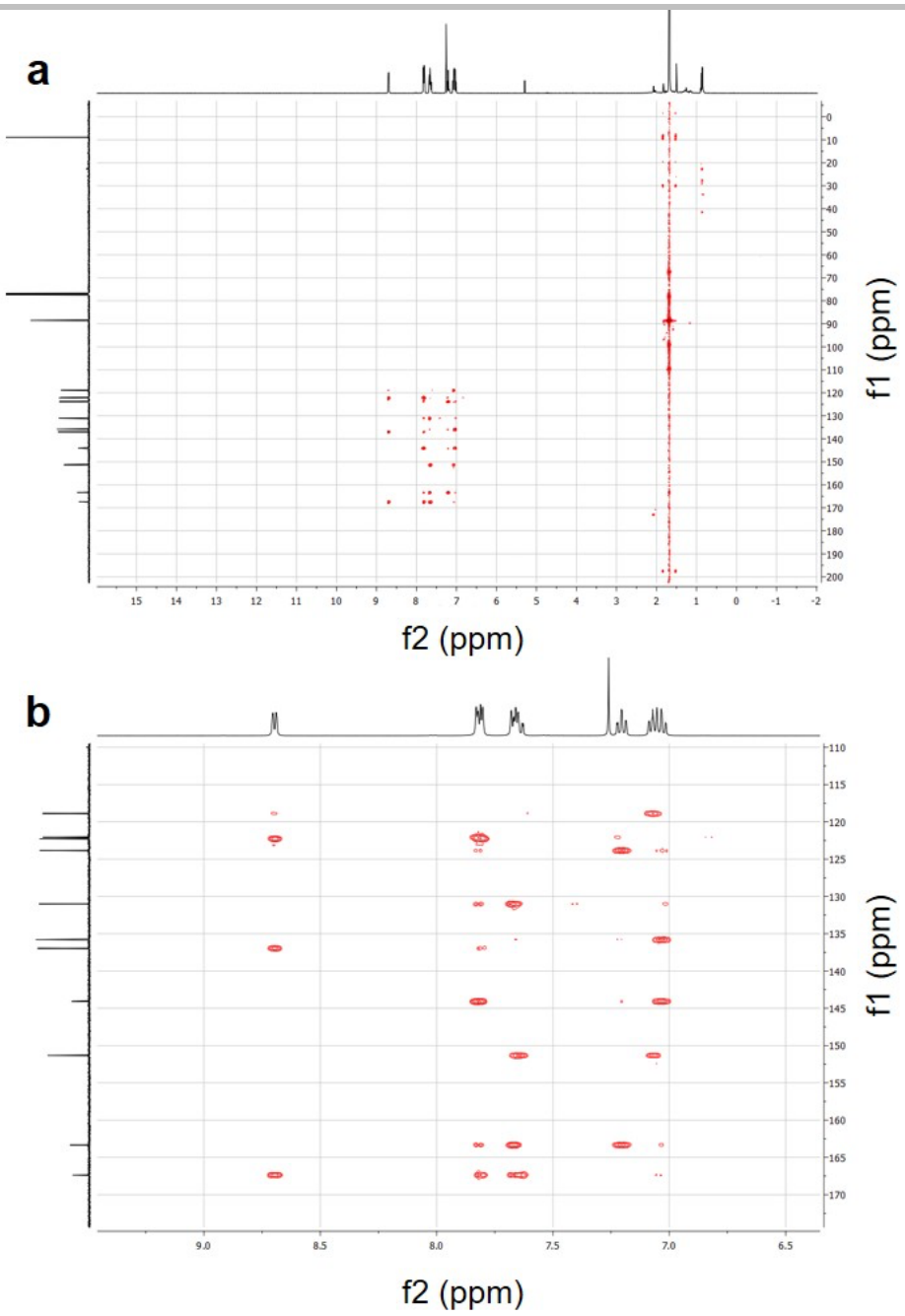


**Figure S11.** HMBC spectrum of IrCp*Cl(2-phenylpyridine) in $CDCl_3$. The lower image shows an enlargement of the aromatic region.

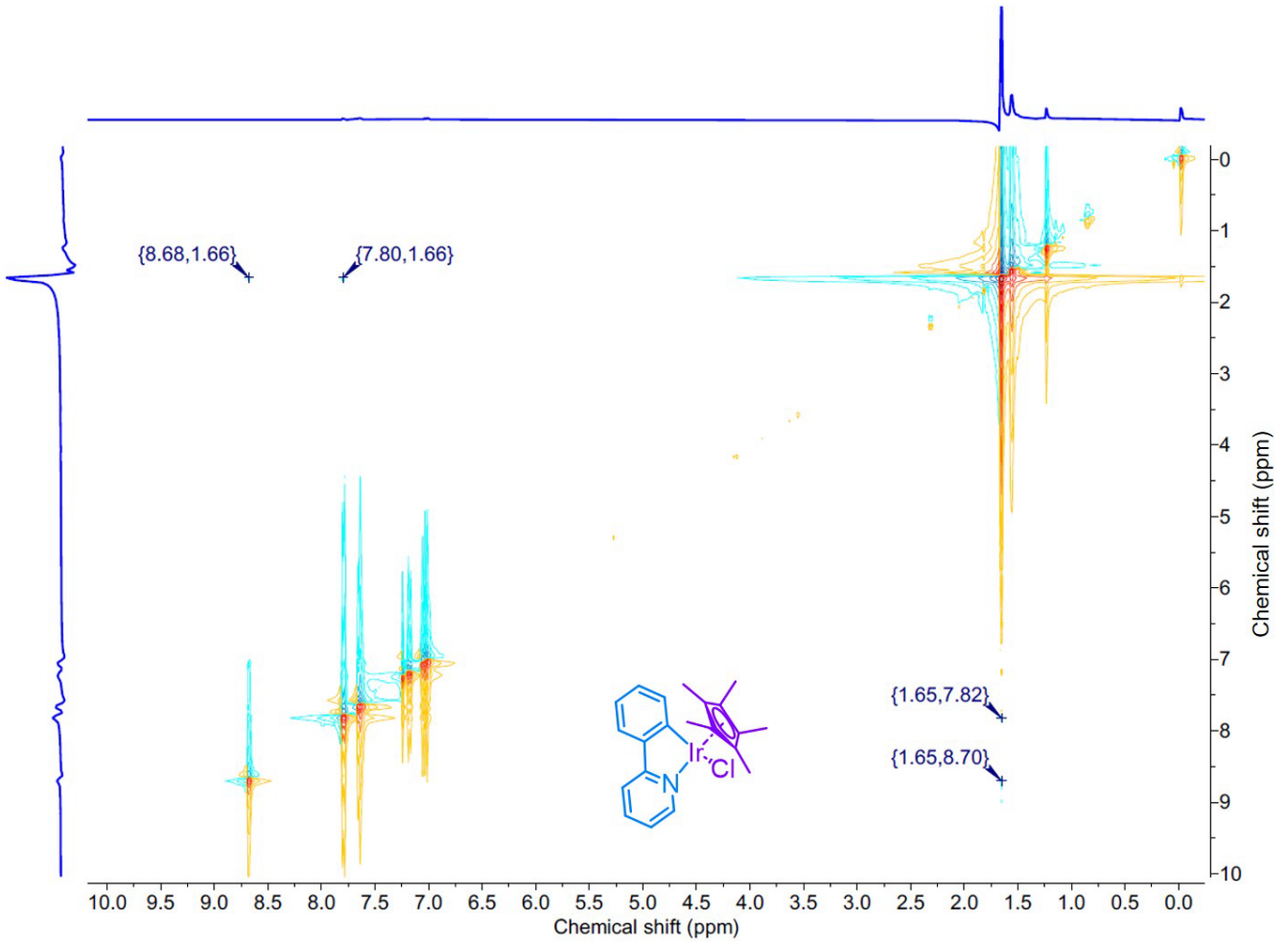


**Figure S12.** NOESY spectrum of IrCp*Cl(2-phenylpyridine) in $CDCl_3$.

To further support the formation of the cyclometallated Ir-complex, two-dimensional NOESY spectroscopy was performed on the molecular model complex IrCp*Cl(2-phenylpyridine) (Figure S12, ESI). The $^{1}$H-$^{1}$H NOSY spectrum exhibits distinct off-diagonal cross-peaks between the Cp* methyl protons (~1.66 ppm) and aromatic pyridyl resonances at 8.68 and 7.80 ppm, corresponding respectively to the proton ortho to the pyridyl nitrogen and the adjacent aromatic proton of the cyclometallated 2-phenylpyridine moiety. These NOE correlations confirm the close spatial proximity between the Cp* fragment and the coordinated phenylpyridine unit around the Ir center, consistent with the formation of the cyclometallated iridacycle structure.

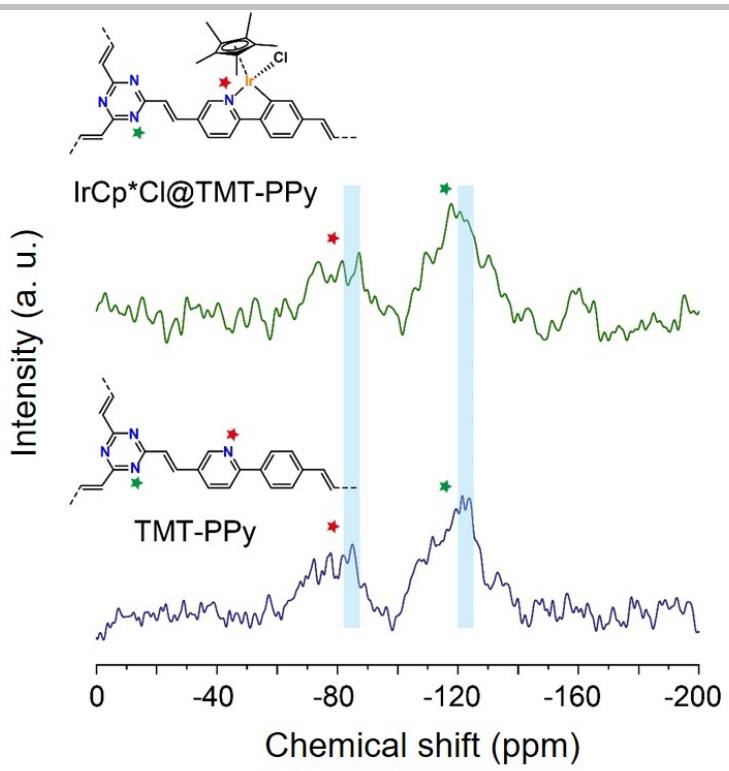


**Figure S13:** $^{15}$N Solid-state cross-polarization magic-angle spinning (CP-MAS) NMR spectral analysis of **TMT-PPy** and **IrCp*Cl@TMT-PPy** COFs.

## Section S-4: X-ray photoelectron spectroscopy (XPS)

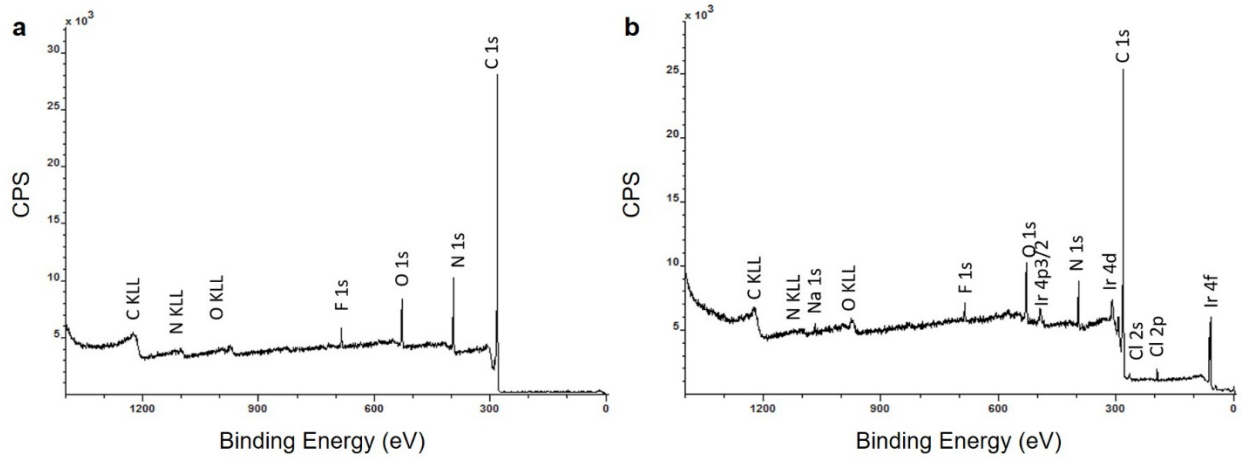


**Figure S14:** X-ray photoelectron spectroscopy (XPS) survey spectrum of a) **TMT-PPy** COF, and **IrCp*Cl@TMT-PPy** COF.

**Section S-5: UV-DRS analysis**

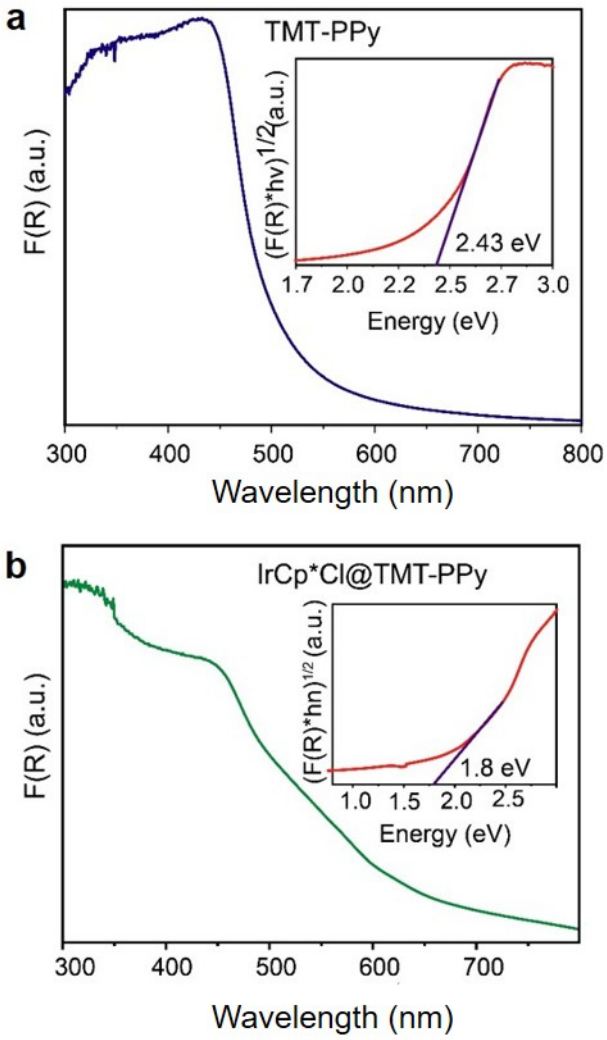


**Figure S15.** UV-DRS spectra of **TMT-PPy** and **IrCp*Cl@TMT-PPy** COFs measured at room temperature (inset: plot showing the *Kubelka-Munk* function to extract the direct optical band gap). A decrease in the band gap was observed upon metalation.

## S-6. $N_2$ and $CO_2$ Sorption studies

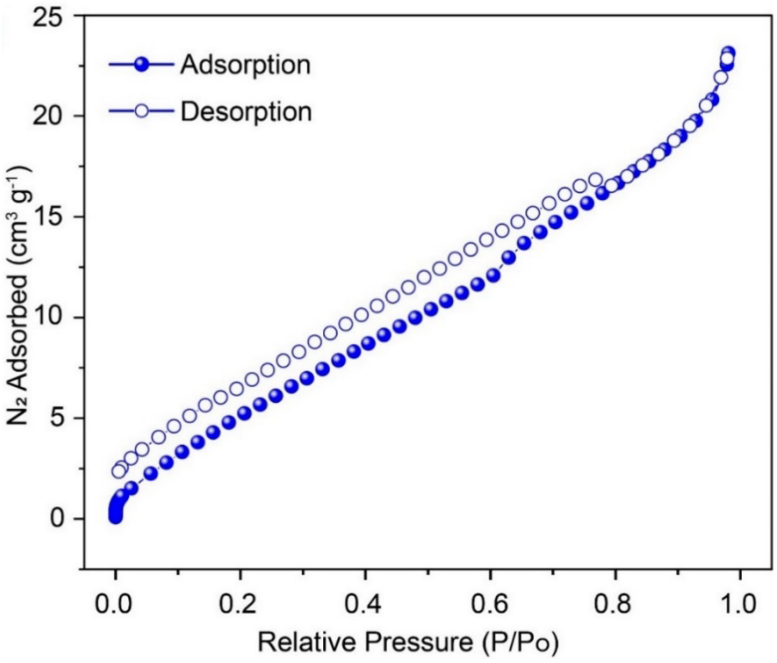


**Figure S16.** $N_2$ Adsorption (solid circles) and desorption (open circles) isotherms of **IrCp*Cl@TMT-PPy** COF recorded at 77 K.

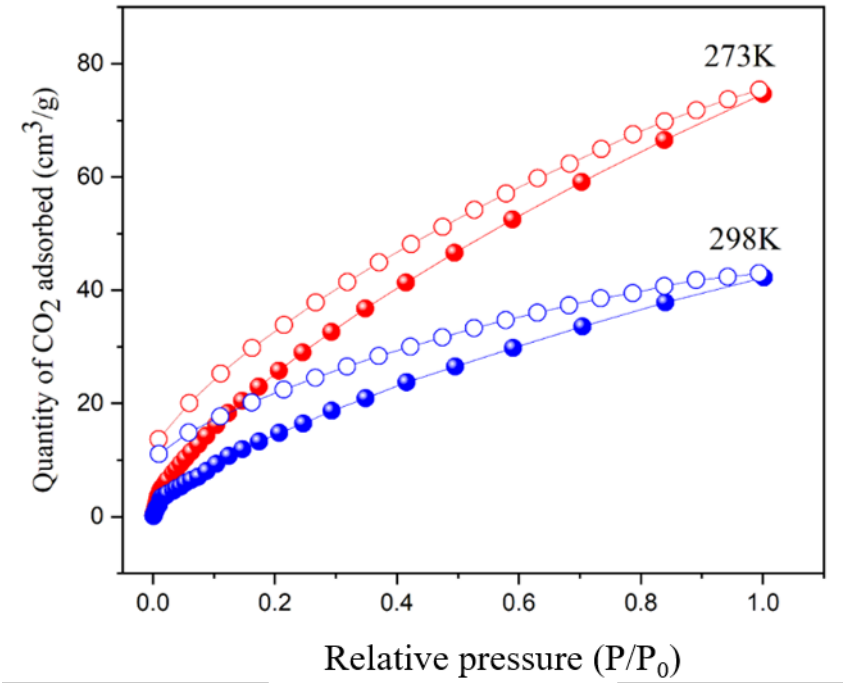


**Figure S17.** $CO_2$ Adsorption (solid circles) and desorption (open circles) isotherms of **TMT-PPy** COF at 273 K (red curve) and 298 K (blue curve). The $CO_2$ isotherms reveal that the total $CO_2$ uptake is 76 $cm^3\ g^{-1}$ and 44 $cm^3\ g^{-1}$ at 273 ºC and 298 ºC, respectively.

## Section S-7: Electron microscopy imaging

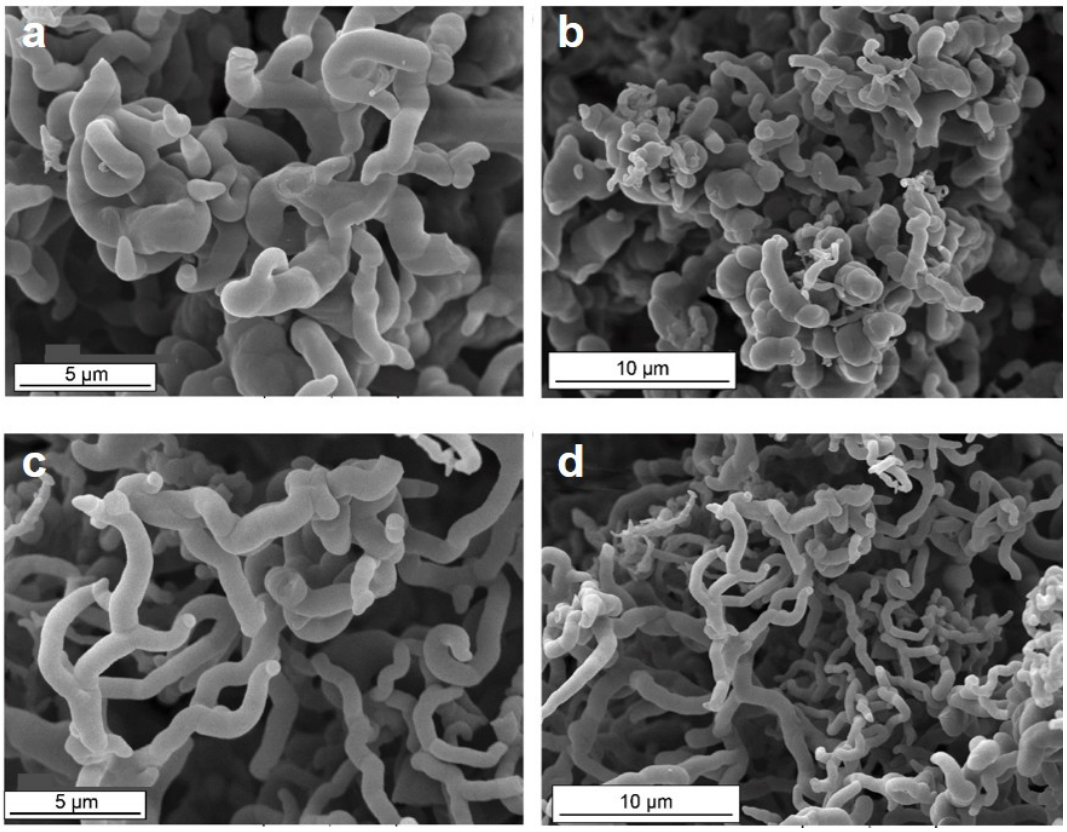


**Figure S18.** Scanning electron microscopy (SEM) images of a, b) **TMT-PPy** and c, d) **IrCp*Cl@TMT-PPy** COFs. Both the COFs exhibit nanofiber morphology in the SEM analysis.

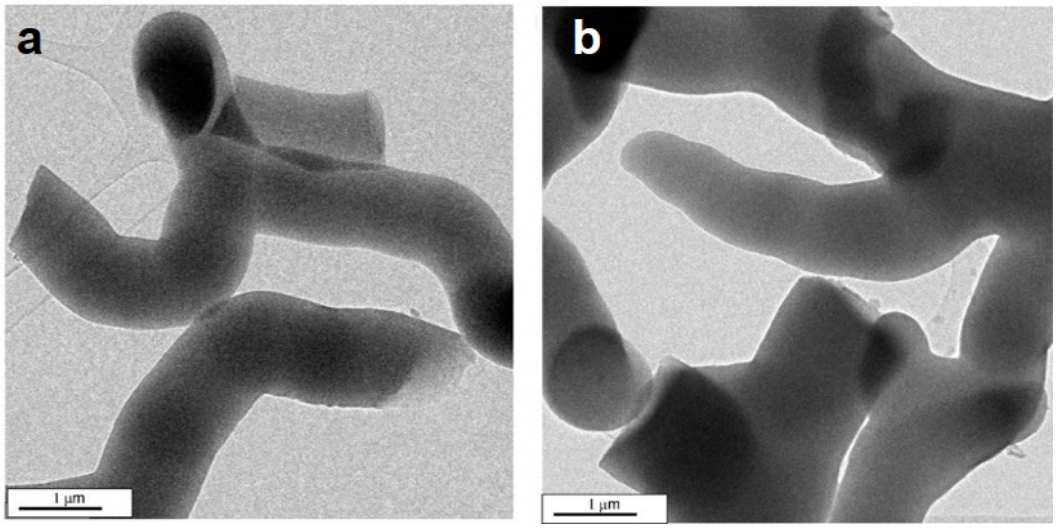


**Figure S19.** Transmission electron microscopy (TEM) images of a) **TMT-PPy** and b) **IrCp*Cl@TMT-PPy** COFs.

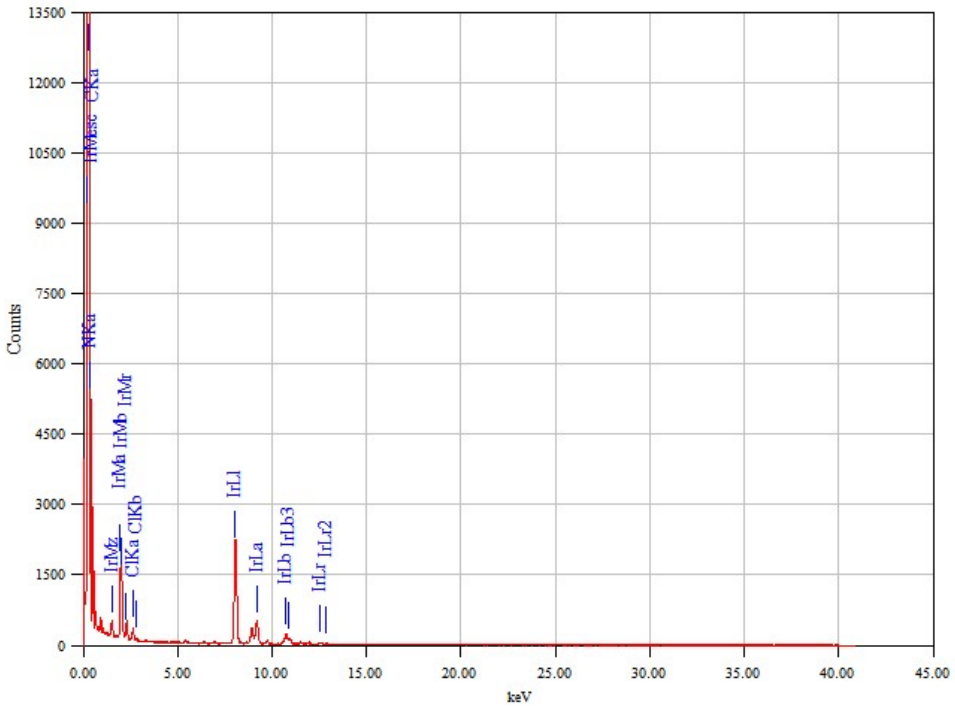


**Figure S20:** TEM-energy dispersive X-ray spectroscopy (TEM-EDS) spectrum of IrCp*Cl@TMT-PPy confirming the presence of Ir together with the framework elements.

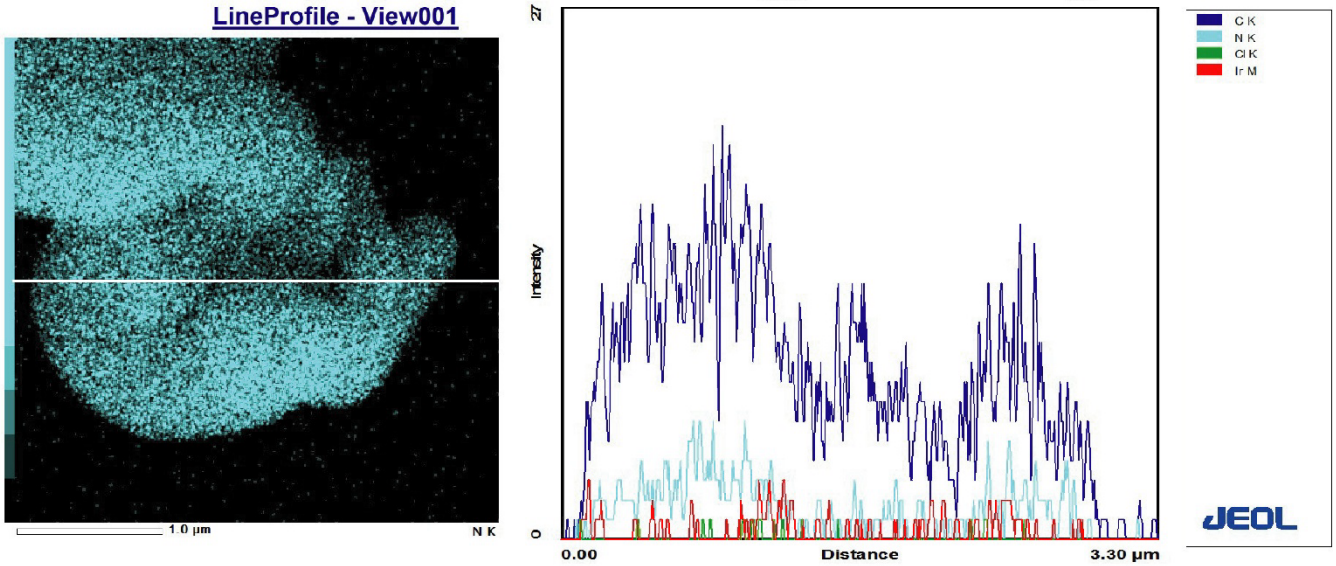


**Figure S21:** EDS line-scan profile of IrCp*Cl@TMT-PPy collected across the selected region, showing the spatial distribution of Ir along the framework.

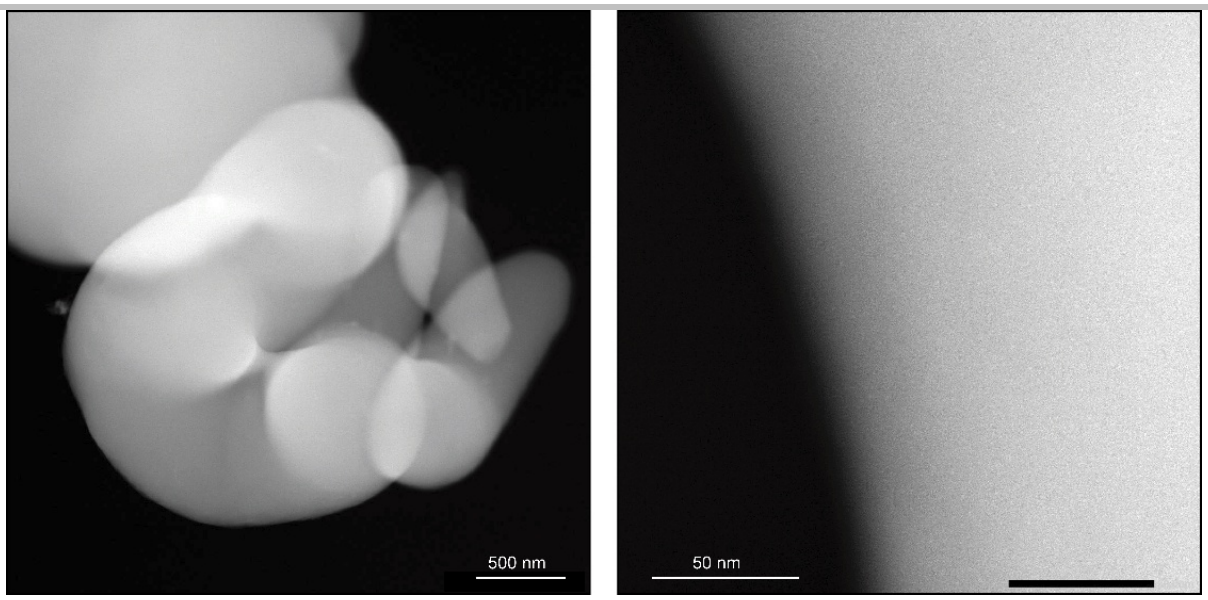


**Figure S22:** HAADF-STEM images of IrCp*Cl@TMT-PPy. The enhanced contrast arising from the high atomic number of Ir supports the dispersion of Ir species within the COF framework without obvious formation of large Ir nanoparticles or aggregates.

TEM-based analyses were performed to investigate the spatial distribution of Ir within the metallated framework. The TEM-EDS elemental mapping images reveal a homogeneous distribution of Ir throughout IrCp*Cl@TMT-PPy without observable phase segregation. The corresponding EDS spectrum confirms the presence of Ir along with the framework elements. Furthermore, EDS line-scan analysis across selected regions shows continuous Ir distribution along the framework. HAADF-STEM images display enhanced contrast arising from the high atomic number of Ir, supporting the dispersion of Ir species within the COF without obvious formation of large Ir aggregates or nanoparticles. These observations collectively support the successful incorporation and uniform dispersion of Ir species within the COF framework.

## Section S-8. Thermogravimetric (TGA) analysis

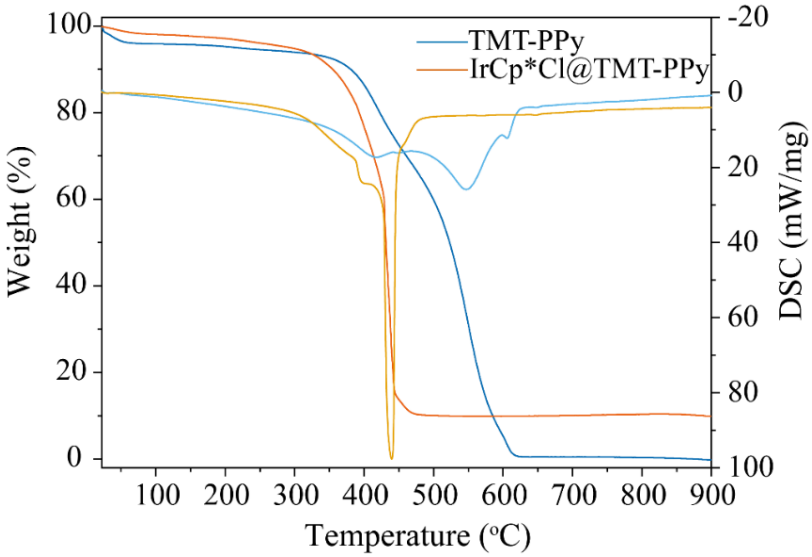


**Figure S23.** Thermogravimetric analysis (TGA) plots of **TMT-PPy** (sky-blue curve) and **IrCp*Cl@TMT-PPy** (orange plot) COFs in the temperature range of 25 – 900 ℃, along with the corresponding differential scanning calorimetry (DSC) curves.

## Section S-9. Synthesis and characterizations of TMT-PP COF

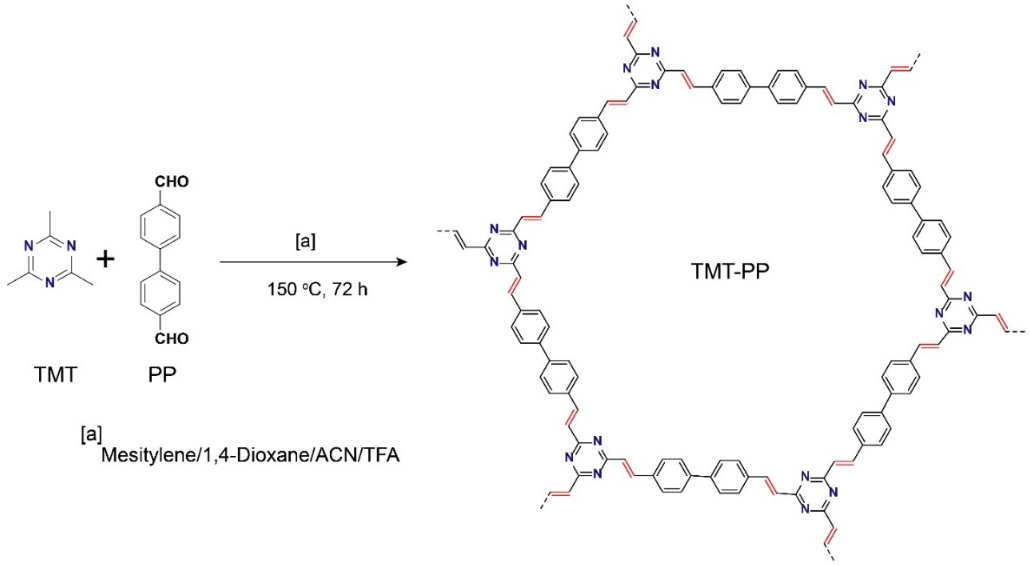


**Figure S24.** Schematic representation of the synthesis of **TMT-PP** COF.

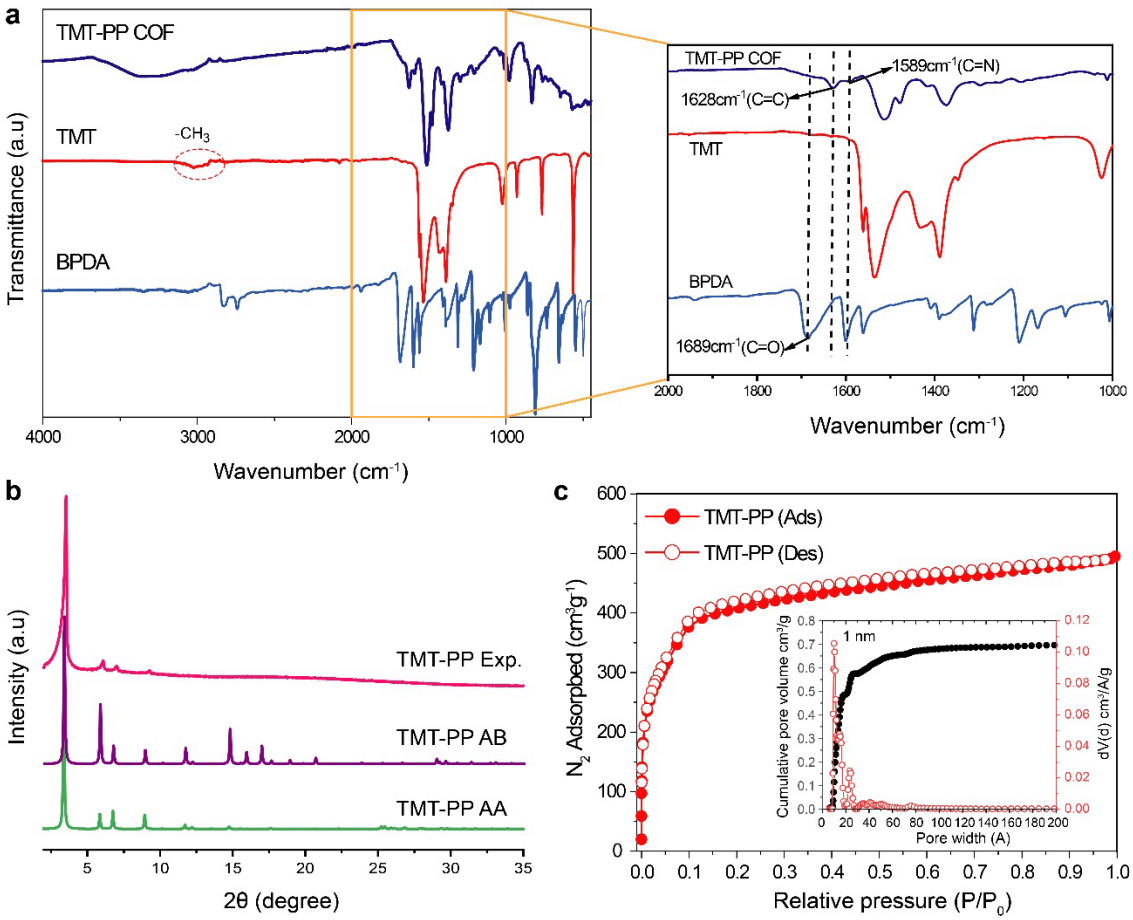


**Figure S25.** a) FT-IR spectra of 2,4,6-trimethyl-1,3,5-triazine (TMT), 4,4'-Biphenyldicarboxaldehyde (PP) monomers and **TMT-PP** COF, b) Experimental (black plot) and simulated AA (red) and AB (sky blue) stacking PXRD patterns of **TMT-PP** COF, and c) $N_2$ Adsorption-desorption isotherms for **TMT-PP** COF recorded at 77 K; inset: calculated pore size distribution of **TMT-PP** COF.

**Section S-10. SQUID Magnetic measurements:**

**SQUID measurements of TMT-PPy COF:**

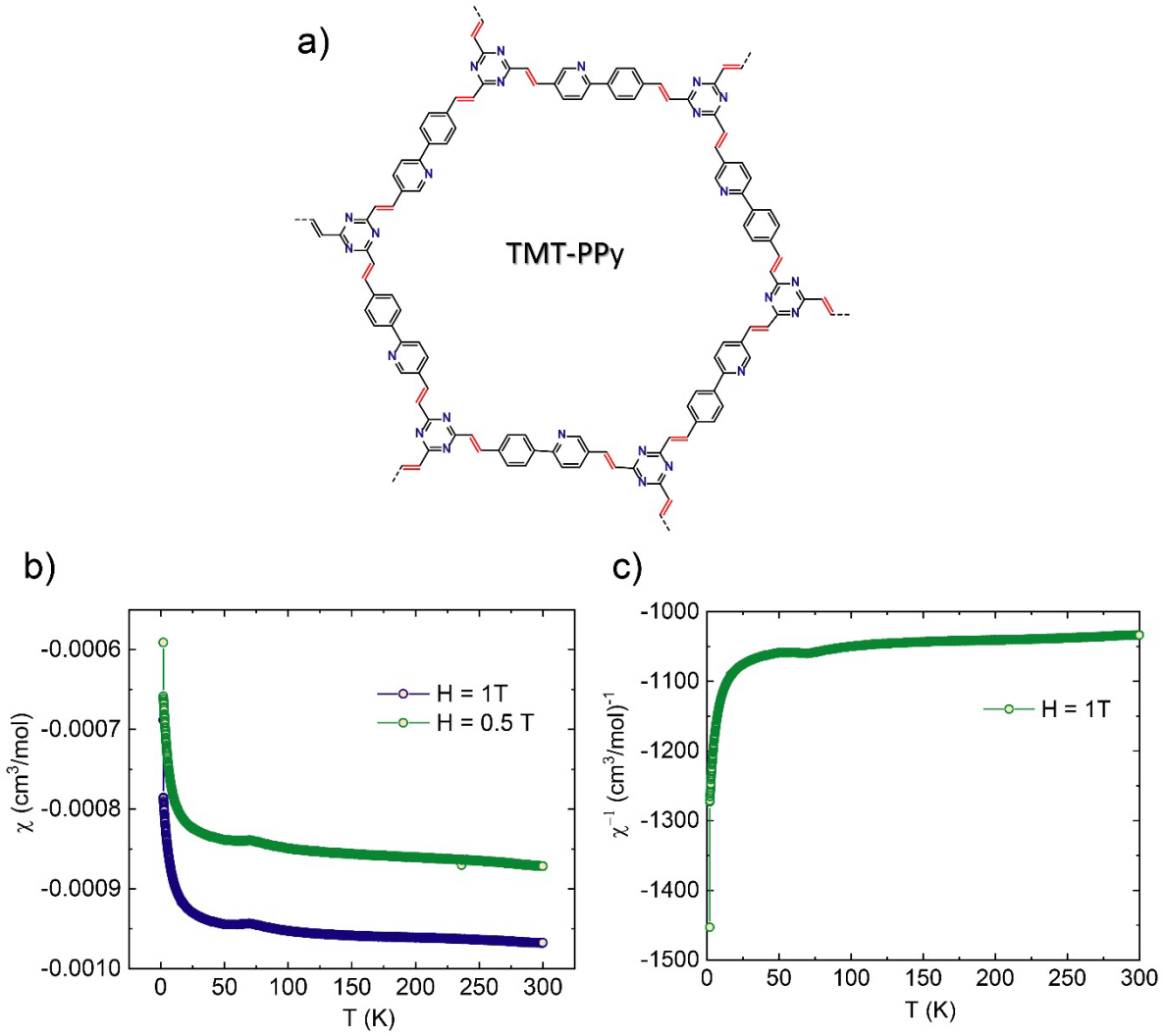


**Figure S26.** SQUID measurements of **TMT-PPy** COF. a) Chemical structure of **TMT-PPy** COF, b) Direct current (*dc*) magnetic susceptibility plots of **TMT-PPy** COF at different field strengths in the temperature range of 2–300 K and c) The temperature dependence of the inverse magnetic susceptibility measured at 1 T in the temperature range 2–300 K.

**SQUID measurements of IrCp*Cl@TMT-PPy COF:**

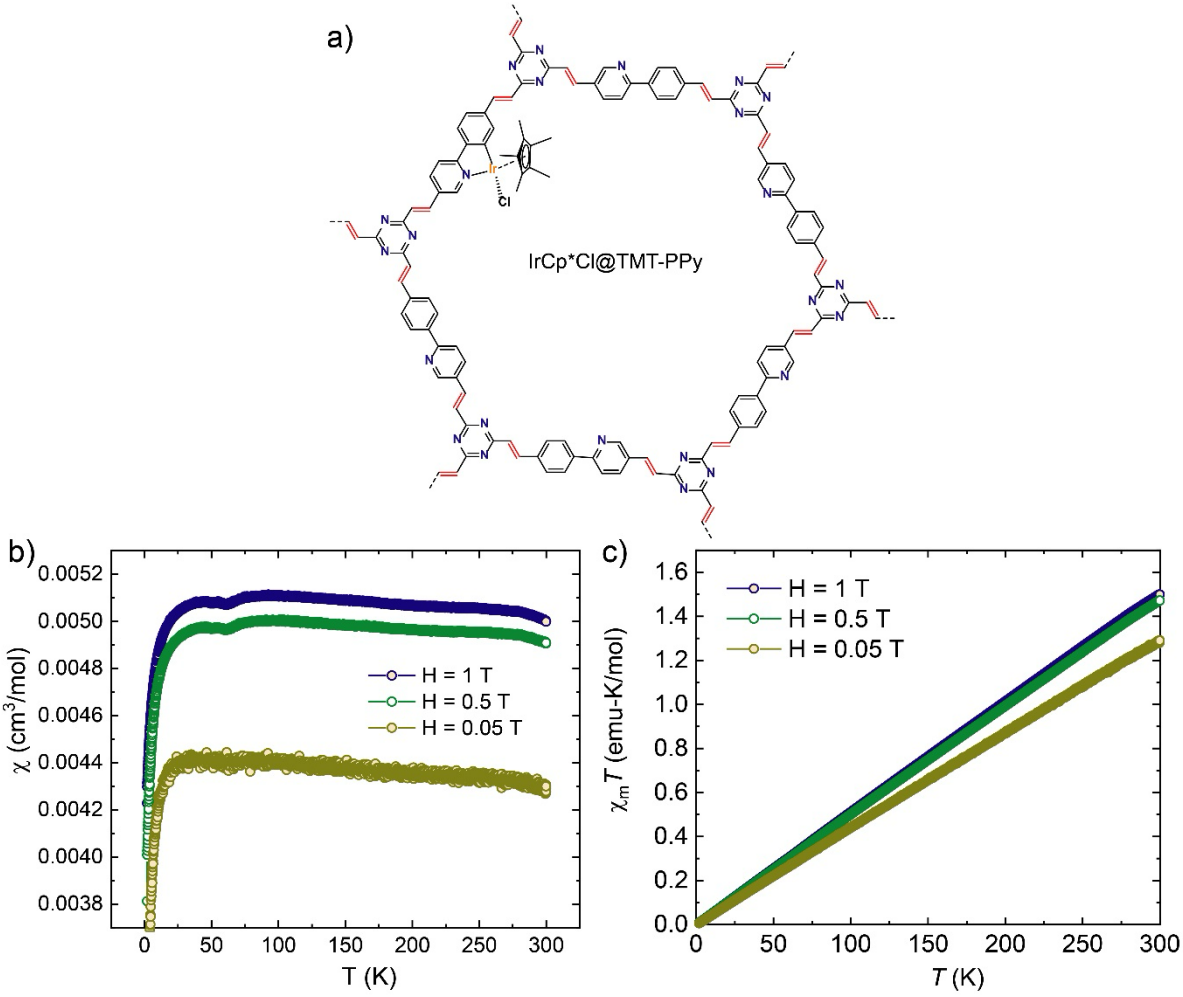


**Figure S27:** SQUID measurements of **IrCp*Cl@TMT-PPy** COF. a) Chemical structure of **IrCp*Cl@TMT-PPy** COF, b) Direct current magnetic susceptibility and c) $\chi_m T$ vs T(K) plots of **IrCp*Cl@TMT-PPy** COF at different field strengths in the temperature range of 2-300 K.

**SQUID measurements of $[IrCp^*Cl_2]_2$ complex:**

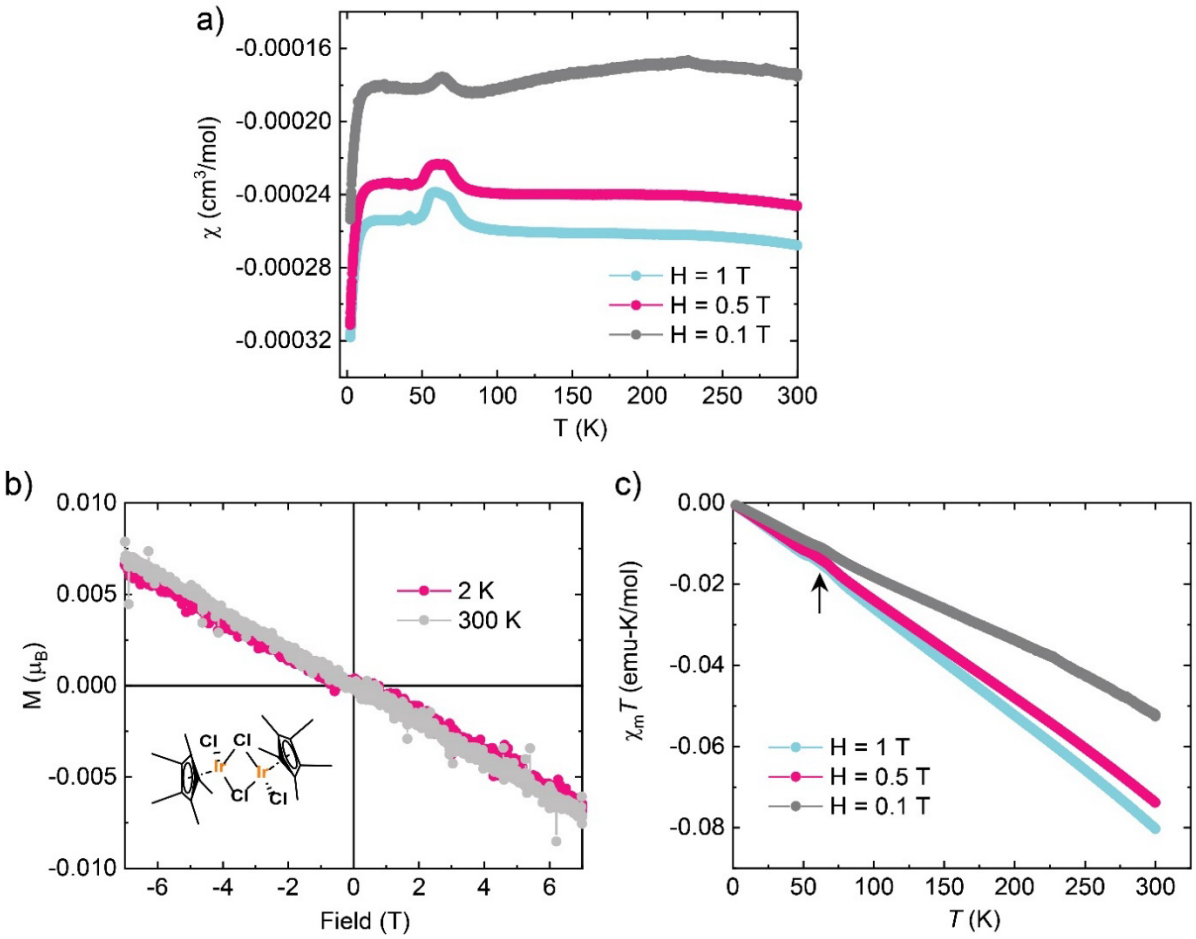


**Figure S28:** SQUID measurements of $[IrCp^*Cl_2]_2$ complex. a) Direct current magnetic susceptibility plots of $[IrCp^*Cl_2]_2$ complex at different field strengths in the temperature range of 2–300 K, b) Magnetization (M) vs field strength (H) curves of $[IrCp^*Cl_2]_2$ complex at 2 and 300 K and c) $\chi_m T$ vs T(K) plots of $[IrCp^*Cl_2]_2$ complex at different field strengths in the temperature range of 2–300 K.

**SQUID measurements of IrCp*Cl(2-phenylpyridine) complex:**

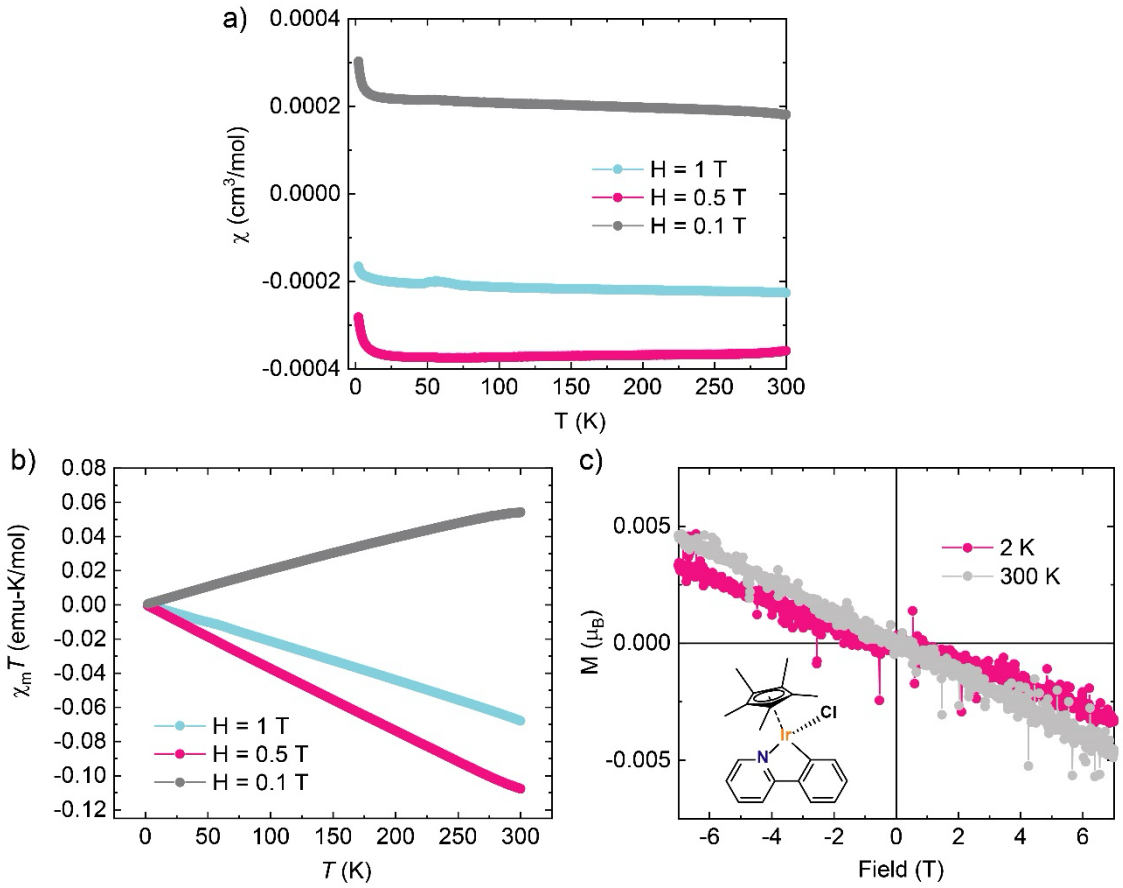


**Figure S29**. SQUID measurements of IrCp*Cl(2-phenylpyridine) complex. a) Direct current magnetic susceptibility curves at different field strengths in the temperature range of 2–300 K, b) $\chi_m T$ vs T(K) plots of IrCp*Cl(2-phenylpyridine) complex at different field strengths in the temperature range of 2 – 300 K and c) Magnetization vs field strength curves (H) of IrCp*Cl(2-phenylpyridine) complex at 2 and 300 K.

**SQUID measurements of TMT-PP COF:**

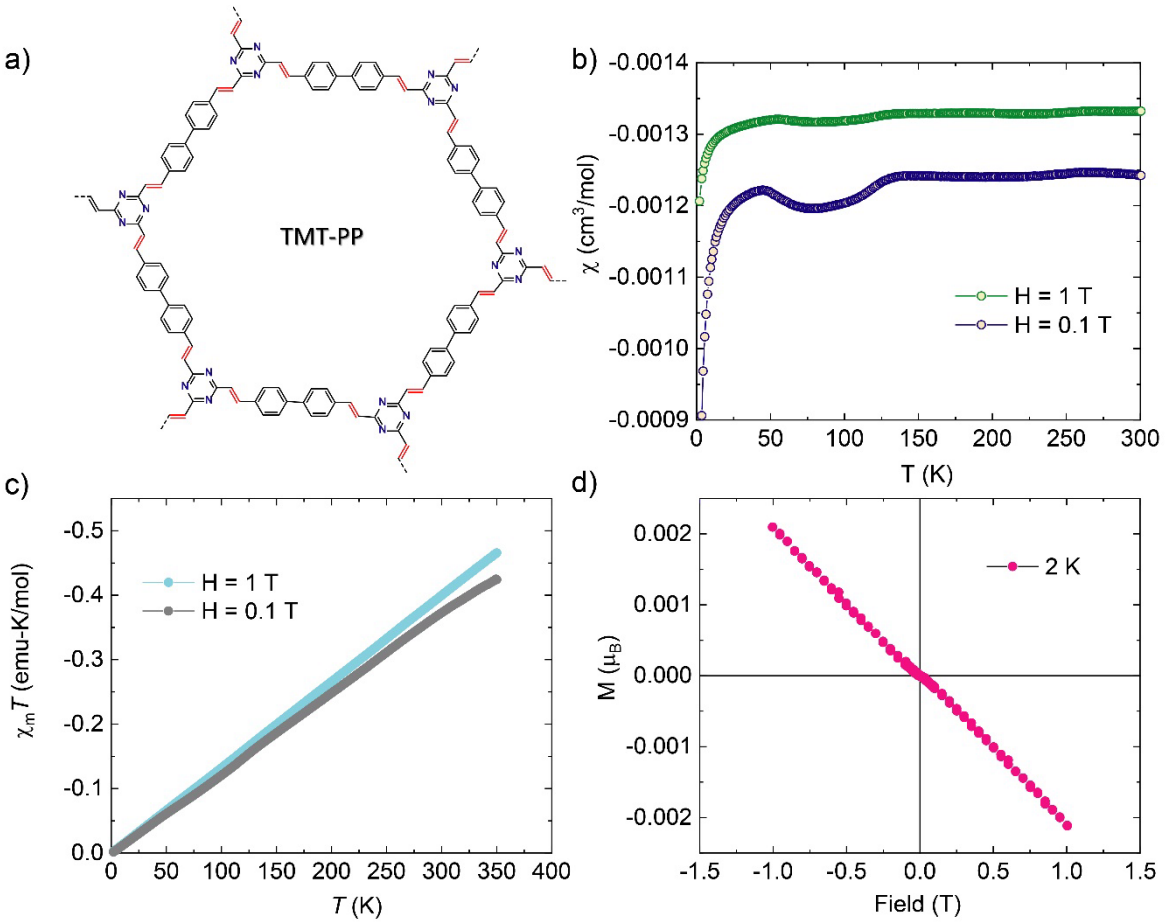


**Figure S30.** SQUID measurements of **TMT-PP** COF. a) Chemical structure of **TMT-PP** COF, b) Direct current magnetic susceptibility plots at different field strengths in the temperature range of 2 – 300 K, c) $\chi_m T$ vs T(K) plots of **TMT-PP** COF at 0.1 and 1T in the temperature range of 2–300 K and d) Magnetization (M) vs field strength (H) curves of **TMT-PP** COF at 2K.

**SQUID measurements of TTA-PPy COF:**

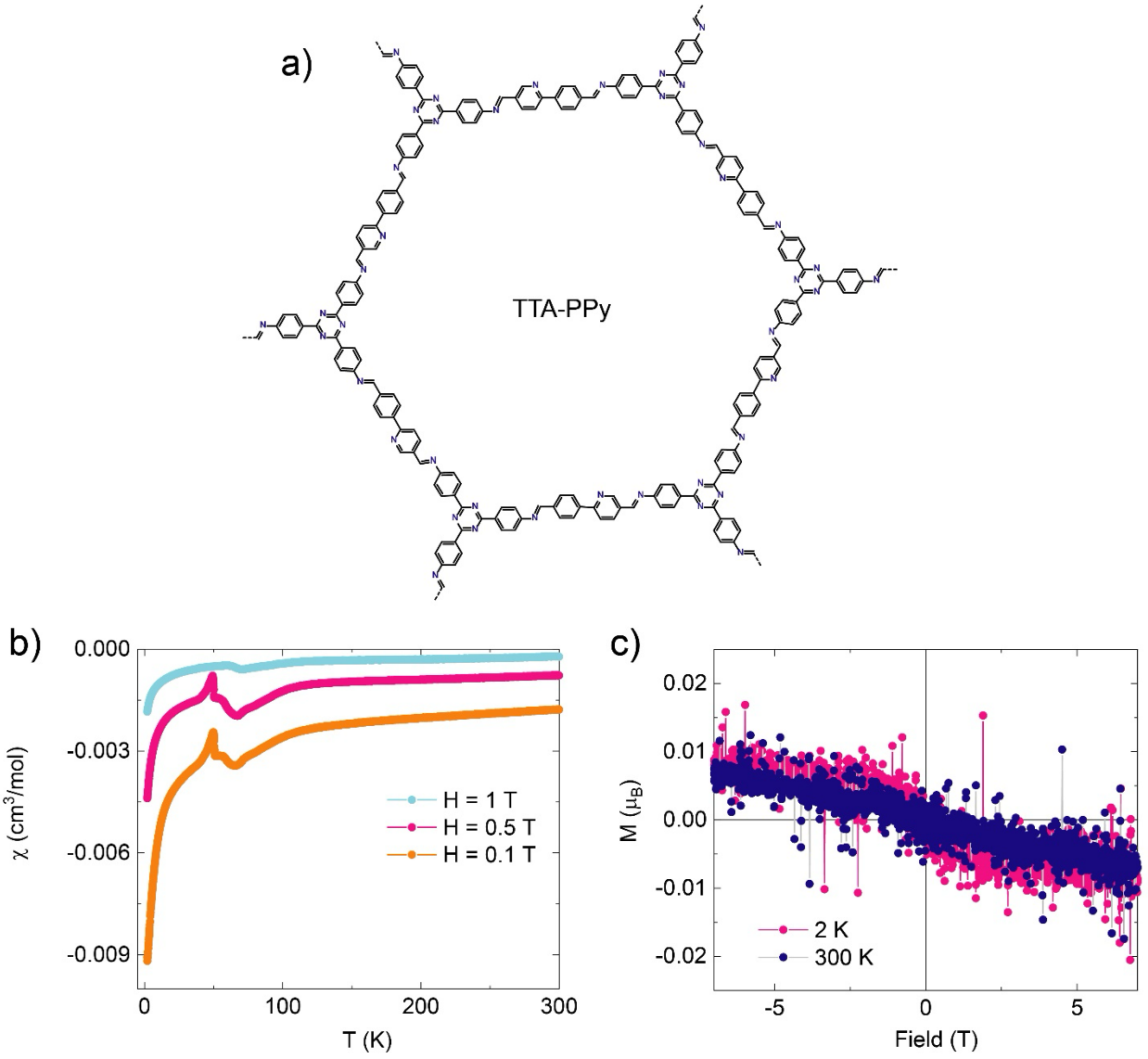


**Figure S31.** SQUID measurements of **TTA-PPy** COF. a) Structural representations of **TTA-PPy** COF, b) Direct current magnetic susceptibility plots at different field strengths in the temperature range of 2–300 K and b) Magnetization (M) vs field strength (H) curves of **TTA-PPy** COF at 2 K and 300 K.

**SQUID measurements of IrCp*Cl@TTA-PPy COF:**

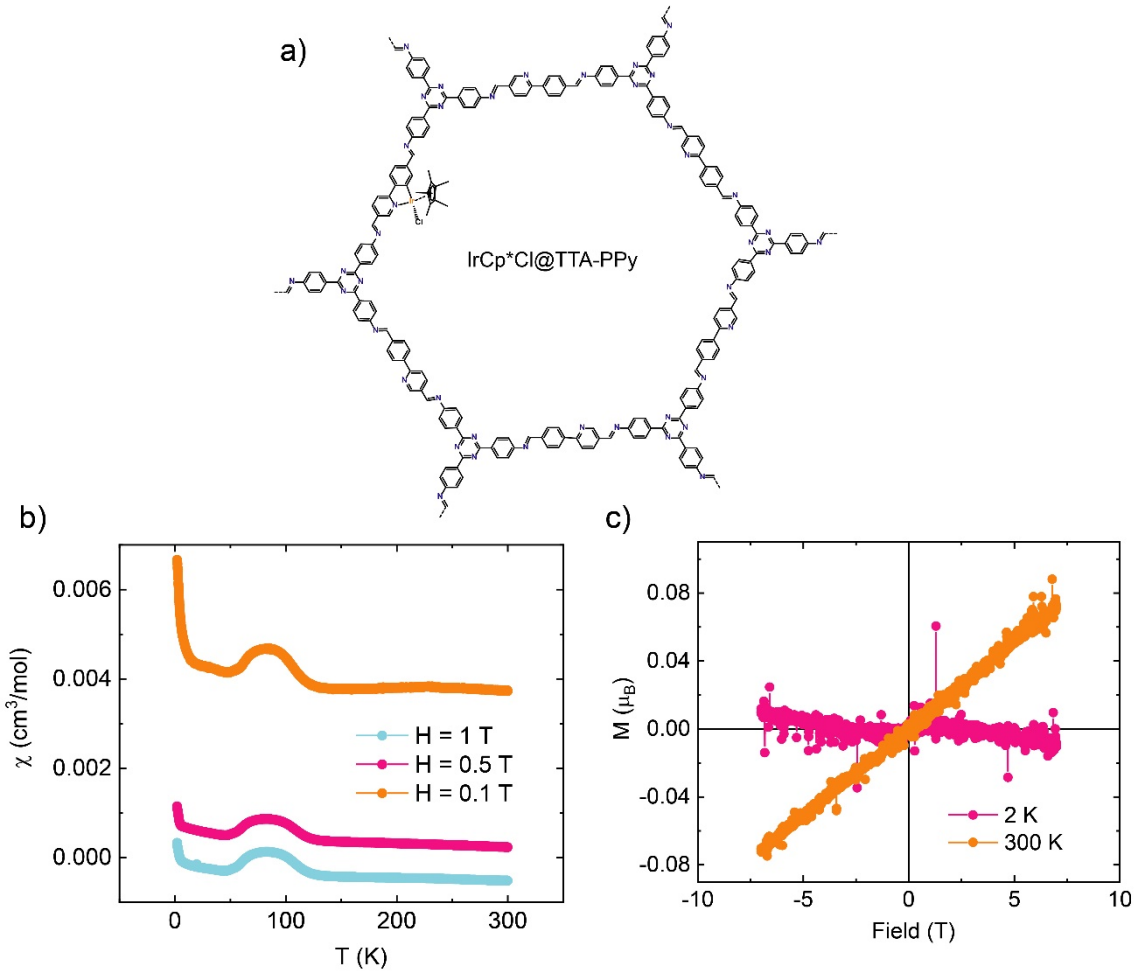


**Figure S32.** SQUID measurements of **IrCp*Cl@TTA-PPy** COF. a) Chemical structure of **IrCp*Cl@TTA-PPy** COF, b) Direct current magnetic susceptibility plots at different field strengths in the temperature range of 2-300 K and c) Magnetization (M) vs field strength (H) curves of **IrCp*Cl@TTA-PPy** COF at 2 K and 300 K.

**Comparison of the magnetic behavior of IrCp*Cl@TMT-PPy and IrCp*Cl@TTA-PPy COFs**

The susceptibility of IrCp*Cl@TTA-PPy COF above 130 K is paramagnetic, as the inverse and the normal susceptibilities are almost temperature-independent. Below 130 K, it shows a very broad peak centered around 55 – 110 K, indicating some short-range magnetic correlations. This magnetic behavior is quite different as compared to IrCp*Cl@TMT-PPy COF because it shows temperature dependency in both normal as well as in inverse susceptibility, and the susceptibility drastically drops at low temperatures, indicating no magnetic impurity in the IrCp*Cl@TMT-PPy COF sample. However, at a lower temperature, the increase in susceptibility is due to Curie's tail, which usually comes from the tiny amount of magnetic impurities found in the IrCp*Cl@TTA-PPy COF. The kink at ~55 – 110 K in IrCp*Cl@TTA-PPy COF susceptibility shows the possible transition of magnetic state. The magnetization vs field strength curves of IrCp*Cl@TTA-PPy COF at 300 K show paramagnetic and at 2 K a very weak moment and is on the verge of a paramagnetic and diamagnetic state.

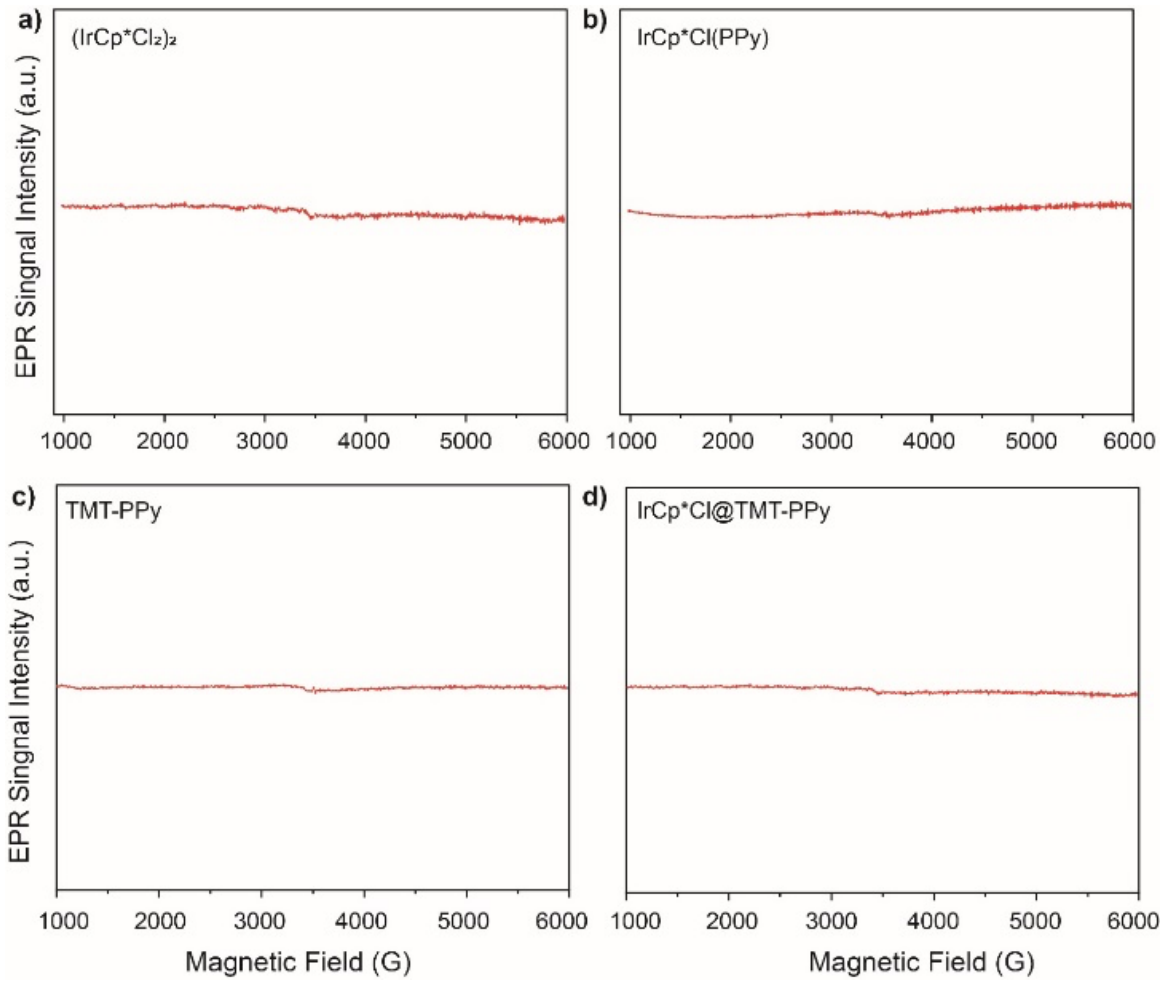


**Figure S33.** EPR Spectra of a) $[IrCp^*Cl_2]_2$, b) IrCp*Cl(2-phenylpyridine) (model compound), c) **TMT-PPy** COF and d) **IrCp*Cl@TMT-PPy** COF at room temperature.

## Section S-11. Theoretical Analysis

Density functional theory (DFT)[3] calculations were performed using the Gaussian 16 program[4] with the unrestricted B3LYP functional and the def2-SVP basis set.[5] To investigate both the local electronic structure of the Ir center and the possible magnetic interactions between neighbouring Ir sites, two molecular models were considered: (i) a single-site molecular model representing the local coordination environment of an isolated IrCp*Cl unit anchored to the pyridyl moiety, and (ii) a two-site Ir(III) model containing two IrCp*Cl units connected through a conjugated linker to approximate possible framework-assisted magnetic interactions within the COF. All molecular structures were fully optimized in the gas phase, followed by vibrational frequency analysis at the same level of theory. The absence of imaginary frequencies confirmed that the optimized geometries correspond to minima on the potential energy surface. All reported energies of the optimized structures include zero-point energy (ZPE) corrections, as summarized in Table S2. The calculated singlet-triplet energy gaps (ΔE) indicate that the singlet state is energetically more stable than the triplet state for both the model-1 and model-2 systems. These results indicate that the Ir centers remain predominantly low-spin in nature, while still allowing the possibility of weak electronically perturbed states within the extended framework.

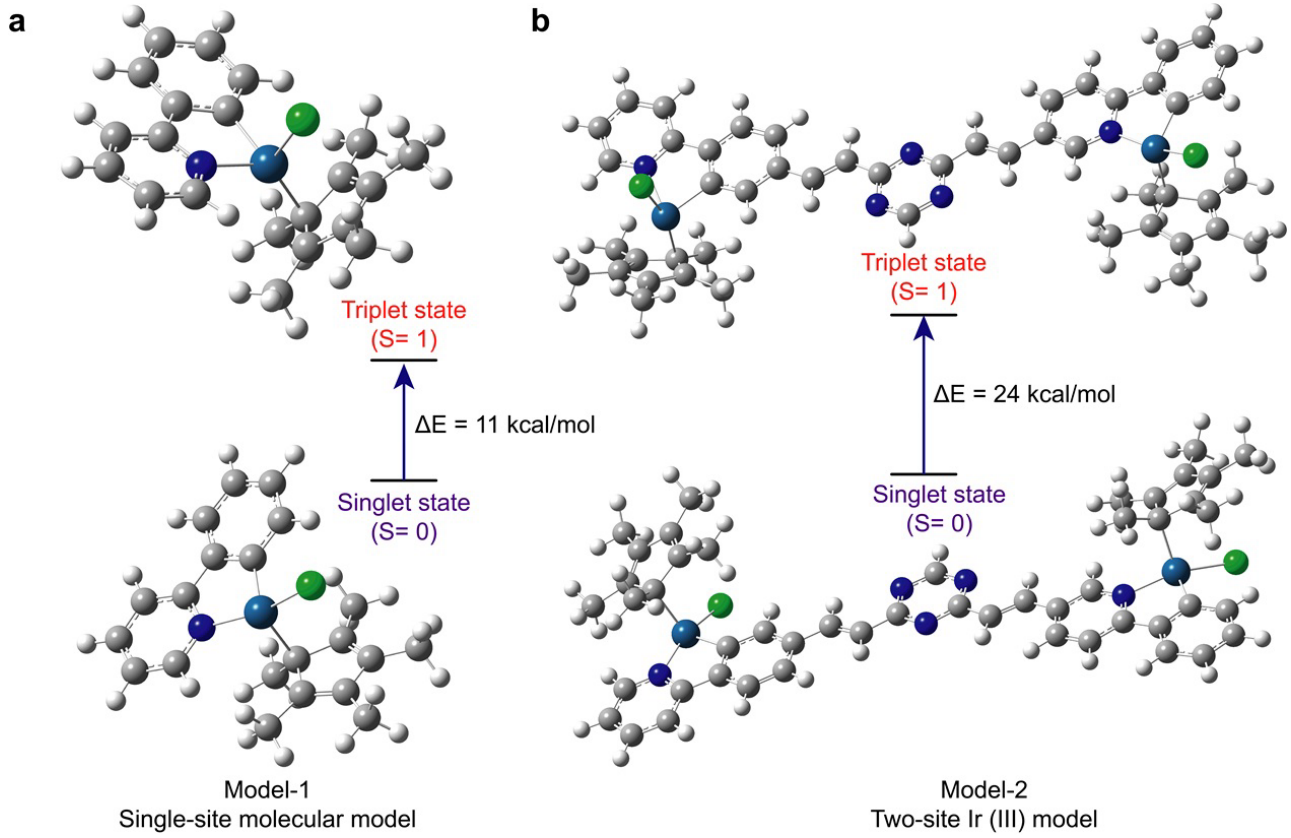


**Figure S34:** DFT optimized structures of the singlet and triplet state of the a) model-1 (single-site molecular model), and b) model-2 (two-site Ir(III) model), with corresponding singlet-triplet energy gaps.

**Table S2:** Optimized structures' energies obtained from uB3LYP/def2-SVP calculations.

| System | Electronic Energy (a.u.) | Zero-point Energy Correction (a.u) | Ground State Energy (a.u.) |
|---|---|---|---|
| Model-1(Singlet) | -1432.728625 | 0.381892 | -1432.346733 |
| Model-1 (Triplet) | -1432.709206 | 0.380424 | -1432.328782 |
| Model-2 (Singlet) | -3297.946953 | 0.856746 | -3297.112784 |
| Model-2 (Triplet) | -3297.928463 | 0.854573 | -3297.07389 |

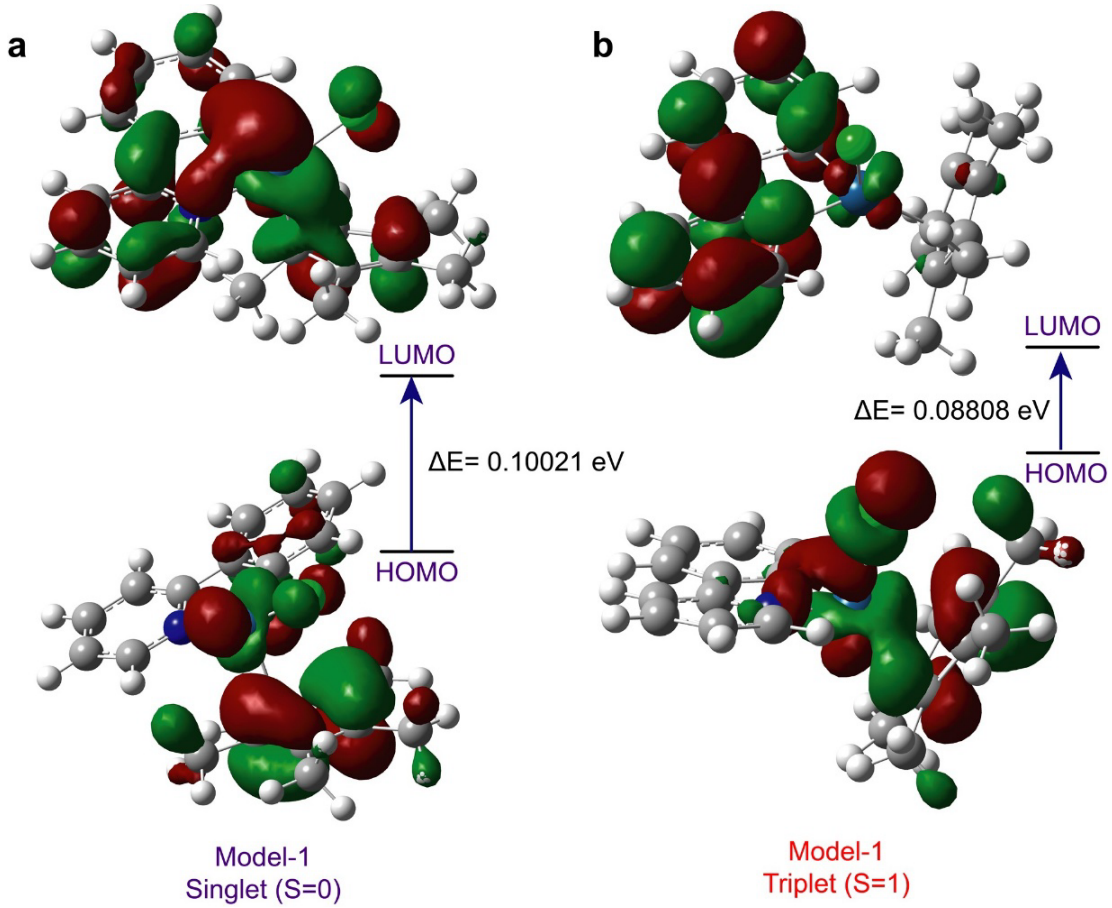


**Figure S35:** HOMO and LUMO orbitals of the a) singlet and b) triplet state of model-1, with corresponding energy gaps.

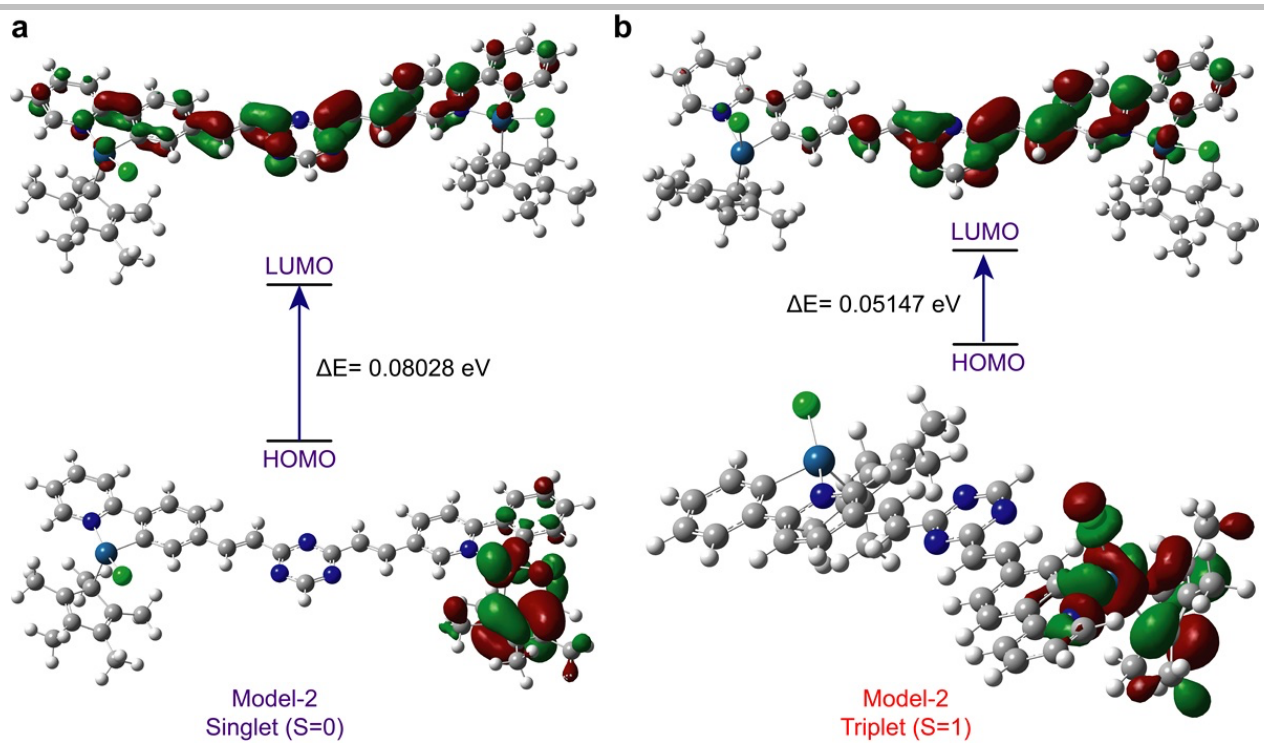


**Figure S36:** HOMO and LUMO orbitals of the a) singlet and b) triplet state of model-2, with corresponding energy gaps.

The HOMO-LUMO energy gaps were calculated and are summarized in Table S3. In both the model-1 and model-2 systems, the triplet state exhibits a smaller HOMO-LUMO gap compared to the corresponding singlet state. Furthermore, upon going from the model-1 to model-2, a significant reduction in the HOMO–LUMO gap is observed for the triplet state. In both model-1 and model-2, the triplet state exhibits a smaller HOMO-LUMO gap relative to the corresponding singlet state. In particular, the pronounced reduction in the HOMO-LUMO gap for the triplet dimer suggests enhanced electronic delocalization across the conjugated framework, which may facilitate weak electronic communication and framework-assisted magnetic interactions between neighboring Ir centers.

**Table S3**: Calculated HOMO and LUMO energies along with the corresponding HOMO–LUMO gaps for the singlet and triplet states.

| System | HOMO (eV) | LUMO (eV) | ΔE (eV) |
|---|---|---|---|
| Model-1 (Singlet) | -0.18528 | -0.08507 | 0.10021 |
| Model-1 (Triplet) | -0.15262 | -0.06454 | 0.08808 |
| Model-2 (Singlet) | -0.18564 | -0.10536 | 0.08028 |

| | | | |
|---|---|---|---|
| Model-2 (Triplet) | -0.15469 | -0.10322 | 0.05147 |

Spin-density analysis of the triplet-state geometries further supports the possibility of framework-assisted magnetic interactions. As shown in Figure S37, the unpaired spin density is distributed not only over the Ir center but also partially delocalized onto the surrounding ligand framework. This observation suggests that any magnetic response emerging after metallation is unlikely to arise solely from intrinsic localized moments at isolated Ir(III) sites. Instead, the calculations indicate that partial spin delocalization through the conjugated backbone and weak ligand-mediated interactions may contribute to the experimentally observed magnetic behavior.

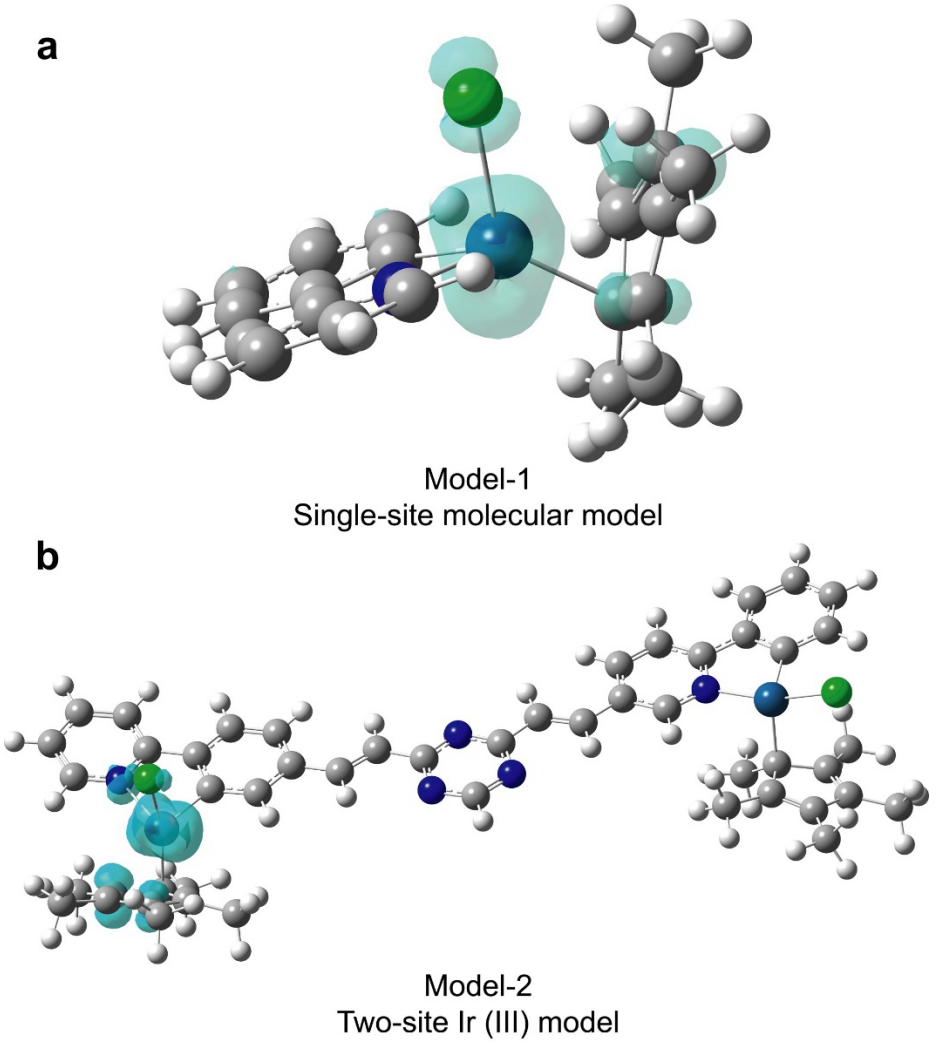


**Figure S37:** Spin density plots of a) model-1, and b) model-2.

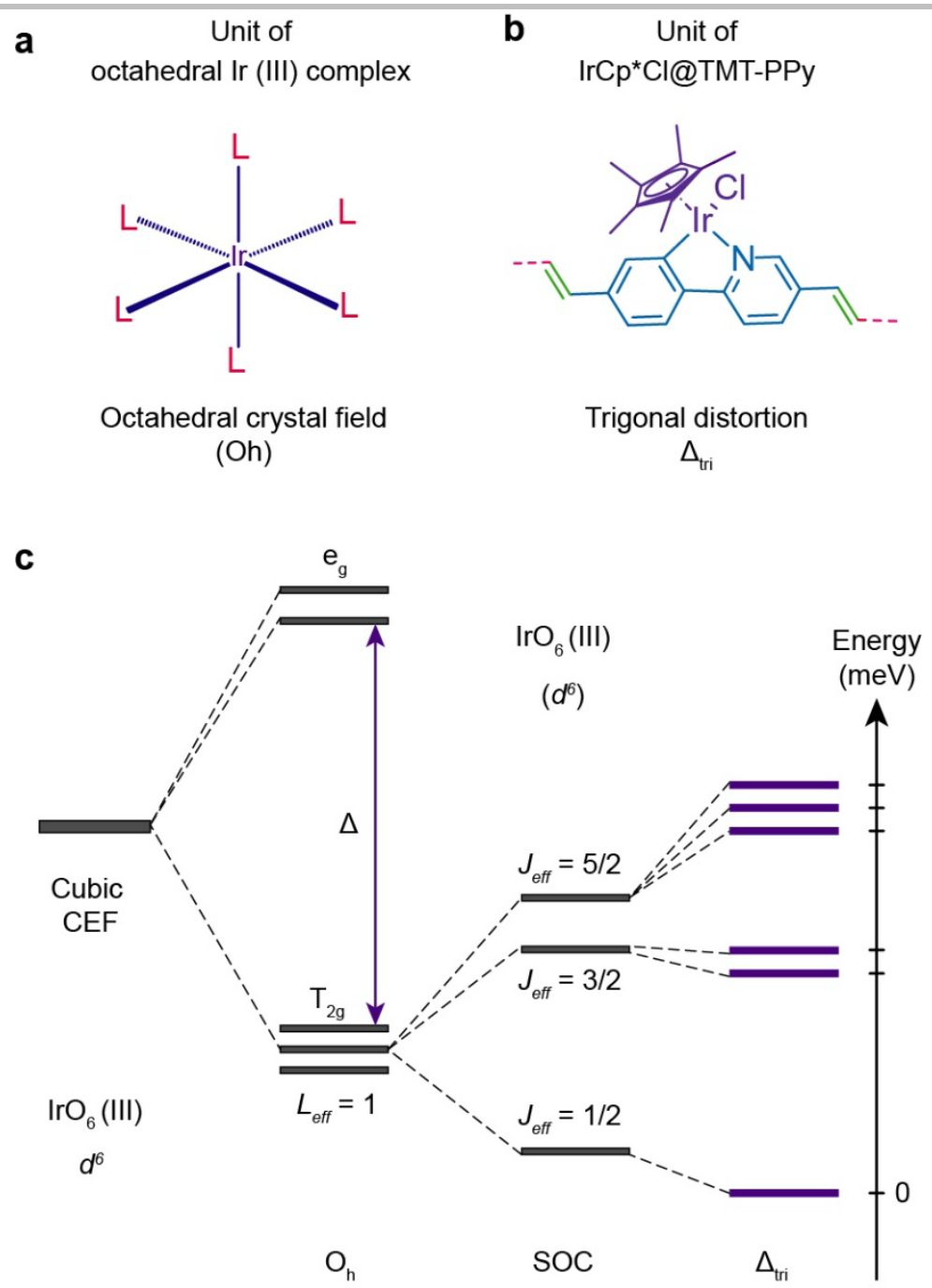


**Figure S38:** a) Schematic representation of an idealized octahedral coordination environment around an Ir center (L = monodentate ligand); b) Representative local coordination environment of Ir in IrCp*Cl@TMT-PPy, illustrating the *piano-stool* type geometry around the Ir center; c) Schematic illustration of 5d orbital energy-level splitting under the combined influence of crystal electric field (CEF), spin-orbit coupling (SOC), and trigonal distortion ($\Delta_{tri}$) in the Ir-coordinated framework.

## Section S-12. References


1. L. Li, W. W. Brennessel and W. D. Jones, *J. Am. Chem. Soc.*, **2008**, *130*, 12414-12419.
2. H. Lyu, C. S. Diercks, C. Zhu and O. M. Yaghi, *J. Am. Chem. Soc.*, **2019**, *141*, 6848-6852.
3. W. Kohn and L. J. Sham, *Phys. Rev.*, 1965, 140, A1133–A1138.
4. M. J. Frisch, G. W. Trucks, H. B. Schlegel, G. E. Scuseria, M. A. Robb, J. R. Cheeseman, G. Scalmani, V. Barone, G. A. Petersson, H. Nakatsuji, X. Li, M. Caricato, A. V. Marenich, J. Bloino, B. G. Janesko, R. Gomperts, B. Mennucci, H. P. Hratchian, J. V. Ortiz, A. F. Izmaylov, J. L. Sonnenberg, D. Williams-Young, F. Ding, F. Lipparini, F. Egidi, J. Goings, B. Peng, A. Petrone, T. Henderson, D. Ranasinghe, V. G. Zakrzewski, J. Gao, N. Rega, G. Zheng, W. Liang, M. Hada, M. Ehara, K. Toyota, R. Fukuda, J. Hasegawa, M. Ishida, T. Nakajima, Y. Honda, O. Kitao, H. Nakai, T. Vreven, K. Throssell, J. A. Montgomery, Jr., J. E. Peralta, F. Ogliaro, M. J. Bearpark, J. J. Heyd, E. N. Brothers, K. N. Kudin, V. N. Staroverov, T. A. Keith, R. Kobayashi, J. Normand, K. Raghavachari, A. P. Rendell, J. C. Burant, S. S. Iyengar, J. Tomasi, M. Cossi, J. M. Millam, M. Klene, C. Adamo, R. Cammi, J. W. Ochterski, R. L. Martin, K. Morokuma, O. Farkas, J. B. Foresman and D. J. Fox, Gaussian 16, Revision C.01, Gaussian, Inc., *Wallingford CT*, *2016*.
5. F. Weigend and R. Ahlrichs, *Phys. Chem. Chem. Phys.*, **2005**, 7, 3297–3305.